GEOPHYSICS, VOL. 89, NO. 1 (JANUARY-FEBRUARY 2024); P. L1–L20, 26 FIGS., 4 TABLES.
10.1190/GEO2023-0238.1





# Evaluating the effects of velocity models and array configuration on induced seismic event locations in the Permian Basin

Xinding Fang[1], Tianrun Chen[1], Siwei Li[1], Nick Brooks[1], George Knapo[1], Alan R. Huffman[2], Tony Lupo[3], and Rachel Storniolo[4]

## ABSTRACT

In the final months of 2022, two substantial earthquakes with magnitudes exceeding ML 5.0 hit West Texas, USA, causing widespread public concerns about the effect of industrial activities on human and environmental safety. The monitoring of earthquakes in this region is largely based on the data of the public regional seismic array, which consists of stations spaced typically tens of kilometers apart. Accurate hypocenter determination of these induced events is crucial as it provides insight into the triggering mechanism, enabling operators and regulators to develop effective mitigation strategies. However, there are debates regarding the accuracy of the publicly reported induced event data due to discrepancies between public reports of event hypocenters and those determined using local dense arrays operated by private companies. The primary objective of this study is to identify the underlying causes of the discrepancies between results obtained from the public regional array in West Texas and local dense arrays. Through modeling and analysis of field data collected by a local dense array in the Permian Basin, we determine that three critical factors influence the reliability of induced event results. First, the accuracy of the velocity model used for the event location is the most crucial factor. Second, the distance between a station and an event plays a crucial role in determining the sensitivity of the data to the hypocenter depth. Finally, consistency between the observed and modeled wave propagation behavior is crucial for ensuring the validity of the objective function in the inversion. Our findings indicate that it is challenging to obtain reliable hypocenters using a regional sparse array with station spacing on the order of tens of kilometers. The best practice for obtaining an accurate event hypocenter and magnitude is to monitor induced seismicity using a local dense array and process the data with a velocity model that fully characterizes the local basin's geology.

## INTRODUCTION

The rate of seismic activity in major oil and gas production areas has witnessed a significant increase in recent years, as reported by multiple studies (Frohlich et al., 2016; Schultz et al., 2017, 2020, 2023; Keranen and Weingarten, 2018; Skoumal et al., 2020). In the last two months of 2022, two significant earthquakes with magnitudes greater than ML 5.0 have been reported in West Texas, USA, sparking a surge of public concern over the potential impact of industrial activities on human and environmental safety (U.S. Geological Survey, 2023). Accurate monitoring and localization of induced seismic events, which are typically smaller than natural earthquakes, are critical for understanding the triggering mechanism and managing/mitigating the risk of induced seismicity. Because meaningful signals of induced seismicity can only be recorded within a relatively short-to-intermediate distance from the hypocenter (generally less than 100 km), the monitoring of those events relies on the use of local or regional seismic arrays. However, discrepancies between the event locations derived from widely spaced regional monitoring arrays and those determined by more proximal dense local arrays have led to questions about the reliability of publicly reported induced event results (Sheng

Manuscript received by the Editor 6 April 2023; revised manuscript received 25 July 2023; published ahead of production 31 August 2023; published online 5 December 2023.
[1]SensorEra Inc, Houston, Texas, USA. E-mail: xinding.fang@sensorera.tech (corresponding author); tianrun.chen@sensorera.tech; siwei.li@sensorera.tech; nick.brooks@sensorera.tech; george.knapo@sensorera.tech.
[2]HighPeak Energy Inc., Fort Worth, Texas, USA. E-mail: ahuffman@highpeakenergy.com.
[3]SM Energy, Midland, Texas, USA. E-mail: tlupo@sm-energy.com.
[4]Birch Resources, Houston, Texas, USA. E-mail: rachel.storniolo@birchresources.com.

et al., 2022). The Permian Basin, located in West Texas, is one of the most heavily studied areas due to the frequent reports of apparently deep earthquakes that occur much deeper than the known injection of disposed fluids.

According to the Texas Seismological Network (TexNet) earthquake catalog (TexNet, 2023), a significant number of the reported events in the Permian Basin have occurred in the deep basement that is several kilometers below the oil and gas production zones and wastewater injection depths. Some events are even reported to happen at depths greater than 12 km (Sheng et al., 2022). A possible mechanism for triggering these deep events is the vertical transmission of poroelastic stress changes caused by shallow wastewater injection (Zhai et al., 2021). However, a study based on the use of stations close to the events in the Delaware Basin along the Reeves-Pecos County line reveals that the induced events in the studied area occurred directly at the wastewater injection depth, which is significantly above the basement (Sheng et al., 2022). Surface deformations derived from InSAR data also support the theory that induced seismicity in the Delaware Basin is associated with the reactivation of preexisting normal faults caused by wastewater disposal (Pepin et al., 2022). Event depth can be a direct indicator used to determine whether an event is associated with deep or shallow fault systems (Hennings et al., 2021), but the presence of discrepancies in event depth reported by different studies results in disagreement regarding the triggering mechanism. Therefore, investigation of the reliability of the hypocenter results derived from public networks and the dominant factors driving these results is vital for understanding the triggering mechanism of induced seismicity correctly.

Induced seismicity differs from natural earthquakes in not only triggering causations (Zhai et al., 2021) but also monitoring distance that can result in different observed signal characteristics. For instance, three examples of induced seismic events with local magnitudes ranging from 2.0 to 5.4 are provided in Table 1, and Figure 1 shows their locations along with four regional stations within approximately 62 km from the epicenters. Seismic signals from induced events are strong in the frequency range of 2–25 Hz over long distances, as shown in Figure 2 (TexNet, 2023). This observation implies that conventional seismic velocity models (e.g., Kennett and Engdahl, 1991; Porritt et al., 2020) and event location methods developed for teleseismic research based on low-frequency assumptions may not be appropriate for induced seismic studies. Although the 2–25 Hz frequency bandwidth is similar to that of conventional exploration seismology, the acquisition offset in induced seismic monitoring (tens of kilometers) is much greater than that in conventional surface seismic exploration (Li et al., 2020). This increased distance affects the traveltime and amplitude of seismic waves, alters their sensitivity to the earth's structures, and leaves a strong free surface footprint on seismic data. Therefore, it may be necessary to adjust the knowledge gained from natural earthquake and microseismicity studies (e.g., Song et al., 2019; Duan et al., 2022) before applying it to the study of induced seismicity.

The objective of this study is to document and evaluate the reasons for the discrepancies in hypocenter results derived from the public regional array and nearby local arrays in the Permian Basin. To achieve this, we begin by using numerical simulations to assess the features of the induced seismic wavefield and how acquisition and processing setups impact hypocenter inversion. Subsequently, we use the insights acquired from numerical modeling to analyze a field data set collected from the Permian Basin and discuss potential explanations for the unusually deep earthquakes frequently reported for this region by TexNet and the U.S. Geological Survey.

## SEISMIC MODELING STUDY

### Velocity models used in this study

This research focuses on the study of recent seismicity in Howard County, Texas. HighPeak Energy Inc. has constructed a high-resolution 3D velocity model for Howard County, based on sonic logs, vertical seismic profile (VSP) data, and 3D seismic data. This enables us to build an accurate local velocity model for the studied area. A 1D velocity model (Figure 3a), called the Howard County 1D (HC1D) model, is extracted from this 3D model based on the locations of the recorded events to be discussed in the following section. Because Howard County has a generally flat geology with a gentle dip from east to west, a 1D layered model can be a suitable approximation for this study. In addition to the HC1D model, a smoothed model called HC1DS is generated by using a 600 m moving window to smooth the HC1D model from 0 to 4 km, as shown in Figure 3b. Figure 3c shows the IASP91 and Delaware Basin 1D

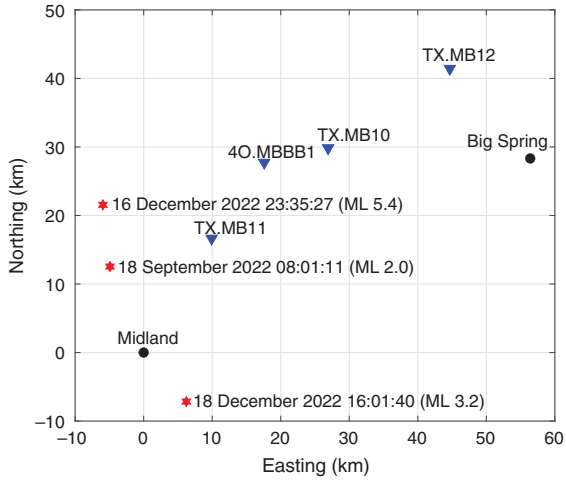


Figure 1. Locations of the events listed in Table 1 relative to Midland City and four nearby stations.

**Table 1. Three induced seismic event examples downloaded from TexNet (TexNet, 2023).**

| Magnitude | Origin time (UTC) | Latitude (°) | Longitude (°) | Depth relative to the ground (km) |
|---|---|---|---|---|
| ML 2.0 | 18 September 2022 08:01:11 | 32.110 | −102.130 | 8.7 |
| ML 3.2 | 18 December 2022 16:01:40 | 31.933 | −102.012 | 12 |
| ML 5.4 | 16 December 2022 23:35:27 | 32.191 | −102.141 | 9.1 |

DOI:10.1190/geo2023-0238.1

(DB1D) models (Savvaidis et al., 2019), which are used for inversion comparisons in the following section. The basement layer in the HC1D model extends to a depth of 20 km and then switches to the IASP91 model (Kennett and Engdahl, 1991). In contrast to the IASP91 and DB1D models, which only have a few simple layers with velocities that increase monotonically with depth, the HC1D model displays more detailed velocity variations above the basement layer that represent the local sedimentary geology.

## Seismic modeling and synthetic waveforms

This section presents a seismic modeling study to investigate the propagation characteristics of seismic wavefields in a typical induced seismic monitoring setup.

To generate synthetic full wave seismic waveform data for the HC1D model with a free surface, we use a generalized reflection and transmission coefficient method (Tang and Fang, 2021), which computes the decoupled P-SV and SH wavefields in 1D stratified media (Aki and Richards, 2002). Compared with other numerical methods such as the finite-difference, finite-element, and spectral-element methods, this method is efficient in generating synthetic waveforms at large distances. For simplicity, we assume isotropic elastic media with a constant density of 2400 kg/m$^3$. In the modeling, we use a strike-slip source with a slip direction of 30° to the $x$-axis direction. The source wavelet is a Ricker wavelet with a 10 Hz center frequency, which covers the representative frequency band of induced seismic signals, as shown in Figure 2.

Figure 4 shows the synthetic seismic profiles along the $x$-axis direction for events located at depths of 3 and 4 km. To highlight the onsets of the first-break signals, the traces (the yellow waveforms) at 20 and 40 km offsets are amplified by factors of 5 and 10, respectively, for plotting purposes. The dashed red and blue curves represent the traveltime of the direct arrivals (the P wave in Figure 4a1 and 4b1 and the S wave in Figure 4a2 and 4b2) calculated using ray tracing (Fang and Chen, 2019) for the HC1D and HC1DS models, respectively. Reflected waves' traveltimes are not shown here because their weak amplitude makes them unlikely to be recognized as first-break signals. The arrival times of first-arrived P and S waves in full wave modeling, which are represented by the dashed green curves, can be obtained by examining the vertical and tangential components of the synthetic waveforms. The radial component is not used in this analysis due to the complexity of the coupling between the P and SV waves (Aki and Richards, 2002). Figure 4 shows that the P and S waves have clear and strong first-break signals at 5 and 10 km offsets, making the picking easy and straightforward. At larger offsets, the first breaks become increasingly dispersive, resulting in significant ambiguity in their picking and therefore greater potential errors in event times.

## Ray tracing versus full-waveform modeling

We observe that the ray-tracing traveltime curves (the dashed red and blue curves) match the waveforms' first breaks (the dashed green curve) well within a 10 km offset. However, the discrepancy between the ray tracing and full wave traveltimes increases with an increasing offset beyond a 10 km offset. We conduct a detailed examination of the raypaths to address this issue next.

In Figure 5, the raypaths obtained from the HC1D model demonstrate that the horizontally propagating section within (for the 4 km depth event) or on top of (for the 3 km depth event) the Ellenburger layer has an important contribution to the paths of direct and reflected waves arriving at stations beyond 10 km. The Ellenburger layer, with its high velocity, acts like a waveguide or "seismic tunnel," attracting seismic waves propagating above and below it similar to refracted head waves. One of the fundamental assumptions of ray tracing is the high-frequency assumption, where the seismic wavelength is much smaller than the thickness of a geologic layer. However, in the case of the Ellenburger layer, the P- and S-wave wavelengths are larger than their thickness. This suggests that the horizontally propagating P and S waves travel at effective velocities that should include the influence of the surrounding formations within their sensitivity zones. This phenomenon of seismic waves traveling through a high-velocity layer resulting in attenuation and dispersion is known as the tunneling effect (Deng, 1992).

After examining the raypaths and understanding the seismic tunneling effect, it becomes clear that the traveltime discrepancy between ray tracing and full-waveform modeling for stations beyond 10 km offset can be explained. Essentially, ray tracing with the HC1D model underestimates the P- and S-wave traveltime because it ignores the finite wavelength effect and violates the high-frequency assumption. The influence of the finite wavelength effect is negligible at near offsets, where seismic waves mainly propagate vertically. However, this effect becomes increasingly significant at large offsets because its influence on seismic wave propagation accumulates as the length of the wave path increases.

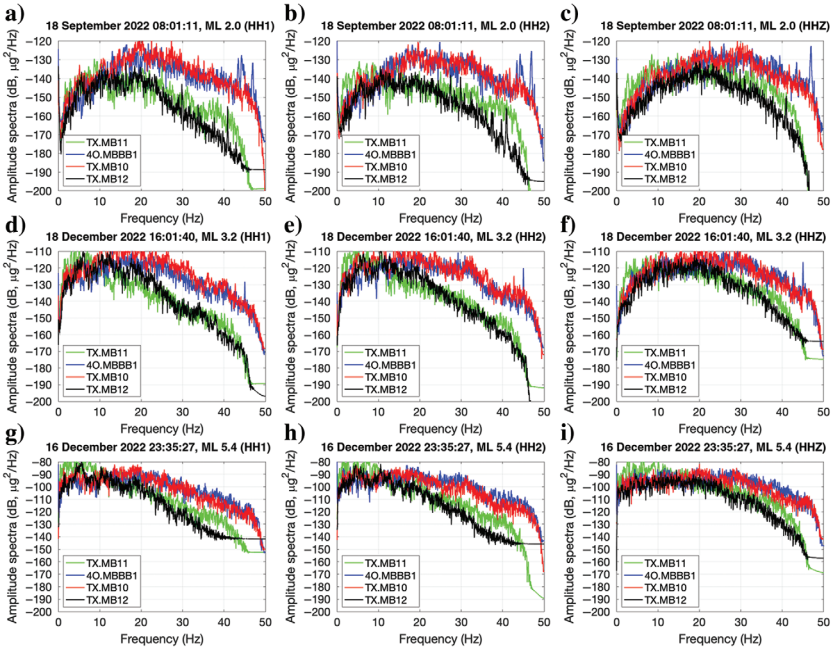


Figure 2. (a–c), (d–f), and (g–i) Comparisons of the spectra of the 3C data recorded at four stations (Figure 1) for the ML 2.0, ML 3.2, and ML 5.4 events, respectively (Table 1); HH1 and HH2 are the two horizontal components and HHZ is the vertical component.

To reduce the influence of high-velocity contrast in ray tracing, a common practice is to smooth the velocity model. As shown in Figure 4 in which the blue curves represent ray-tracing traveltime generated based on the HC1DS model, the traveltime discrepancy between the waveform first breaks and the ray-tracing result is reduced to some extent by smoothing the velocity model. However, smoothing the velocity model is an ad hoc solution that cannot fully address the limitations of ray tracing resulting from finite frequency and fine layering with high-velocity contrasts. In addition, the geometry of the raypaths indicates that the arrival-time differences among stations at large offsets are mainly associated with the differences in the horizontal sections of their raypaths. As a result, the relative traveltimes between distant stations have little sensitivity to the depth of an event, as discussed in detail in the following section.

## Sensitivity of near- and far-offset stations on event depth

To investigate how station distance affects the sensitivity of hypocenter inversion, we create two arrays in the modeling: a near-offset array with four stations at 5, 10, 15, and 20 km offsets, and a far-offset array with stations at 20, 30, 40, and 50 km offsets, as shown in Figure 6. In Figure 7, the waveform-derived traveltime data indicate that the presence of high-velocity layers can introduce negative traveltime gradients and gradient discontinuities in the depth direction. This may cause numerical issues in survey design, hypocenter inversion, relocation, and uncertainty analysis methods that are established based on a traveltime gradient calculation (e.g., Waldhauser and Ellsworth, 2000; D'Alessandro et al., 2011) because calculation of the traveltime gradient's covariance matrix can become numerically singular at the transition depths between positive and negative traveltime gradients. In the following comparisons, differential traveltime is defined as the traveltime relative to the P-wave arrival time of the nearest station in an array (i.e., S1 for the near array and S5 for the far array). We compare differential traveltime instead of absolute traveltime because the event origin time is unknown in the inversion process, and this allows us to decouple hypocenter inversion from origin time inversion. Basically, differential traveltime-based hypocenter inversion is a process of searching for a model-predicted differential traveltime template that can accurately match the observed data. The greater the variations in differential traveltime with respect to event depth, the more sensitive the differential traveltime is to the event depth. Figure 8 compares the differential traveltimes of synthetic waveforms (circles for P waves and triangles for S waves) with those calculated from ray tracing (solid curves for P waves and dashed curves for S waves) for three models, i.e., HC1DS, IASP91, and DB1D. For near stations, the differential traveltime data exhibit a clear variation trend over the entire depth range, indicating that the traveltime data for these stations are highly sensitive to event depth. In contrast, the differential traveltime for the far stations becomes almost vertical within the segments above and below the Ellenburger layer. This indicates that the differential traveltime data for the far stations have very low sensitivity to event depth. Inversion with far stations can easily result in significant depth inversion errors even with small picking ambiguities. For example, as shown in Figure 8b1, a 4 km deep event generates differential traveltime data similar to an event at 10 km depth, making it difficult to obtain a reliable estimate of event depth. This observation presents a critical challenge to regional seismic arrays that are being relied on for operational and regulatory decisions.

We also observe that ray tracing only generates reasonable differential traveltime templates at near stations (Figure 8a1) as the templates (the solid and dashed curves) for the HC1DS model match the waveform first breaks (the circles and triangles) reasonably well for the near stations but deviate for the far stations. For the IASP91 model (Figure 8a2 and 8b2), the P-wave traveltime templates for any events within the basement match well but have poor matching for shallow events. The overall matching of the DB1D model's templates and waveform first breaks is not good, as the DB1D model's velocities do not reflect the layer properties of the HC1D model. In summary, ray tracing is only valid for hypocenter inversion using data from near-offset stations. A full-waveform approach is required to generate differential traveltime

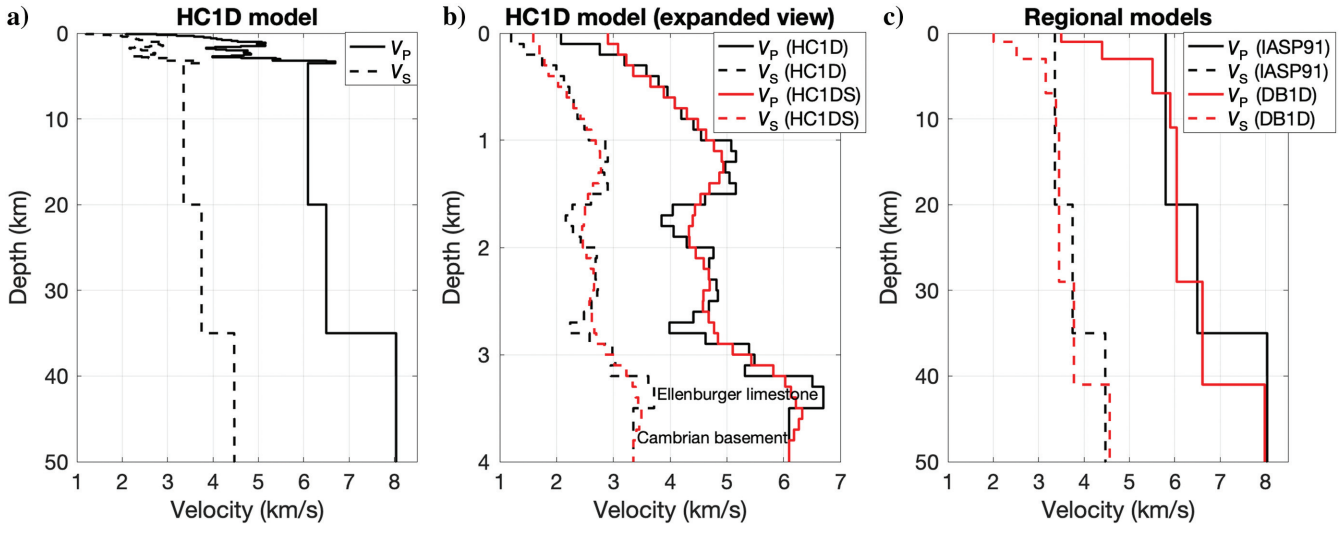


Figure 3. (a) The HC1D model, (b) expanded view of the 0–4 km section of the HC1D model (in black) and the corresponding smoothed model HC1DS (in red), and (c) IASP91 model (in black) and DB1D model (in red). The high-velocity layer overlaying the Cambrian basement in the HC1D model is the Ellenburger limestone formation. Note that the IASP91 model only contains a homogeneous layer above 20 km. The DB1D model is obtained from Figure 6b in Savvaidis et al. (2019).

templates for far-offset stations. In addition, the quality of ray-tracing templates is highly dependent on the accuracy of the velocity model and deteriorates rapidly for far stations.

## Hypocenter inversion using near and far stations

We generate synthetic waveform data using the HC1D model and pick the first-arrival times of P and S waves on the synthetic waveforms as observed data. We then use ray tracing to generate differential traveltime templates based on HC1DS, IASP91, and DB1D models and invert for the event hypocenter with a grid search approach.

The following objective function is minimized through grid search to find the optimal event position:

$$\text{residual} = \sqrt{\frac{\sum_{n=1}^{N_P}(\Delta t_n^P - \Delta T_n^P)^2 + \sum_{n=1}^{N_S}(\Delta t_n^S - \Delta T_n^S)^2}{N_P + N_S}}, \tag{1}$$

with

$$\Delta t_n^P = t_n^P - t_{ref}^P, \tag{2}$$

$$\Delta T_n^P = T_n^P - T_{ref}^P, \tag{3}$$

$$\Delta t_n^S = t_n^S - t_{ref}^P, \tag{4}$$

$$\Delta T_n^S = T_n^S - T_{ref}^P, \tag{5}$$

where $T_n^P$ and $T_n^S$ are the P- and S-wave traveltime picked from the observed data, respectively; $t_n^P$ and $t_n^S$ are the model predicted P- and S-

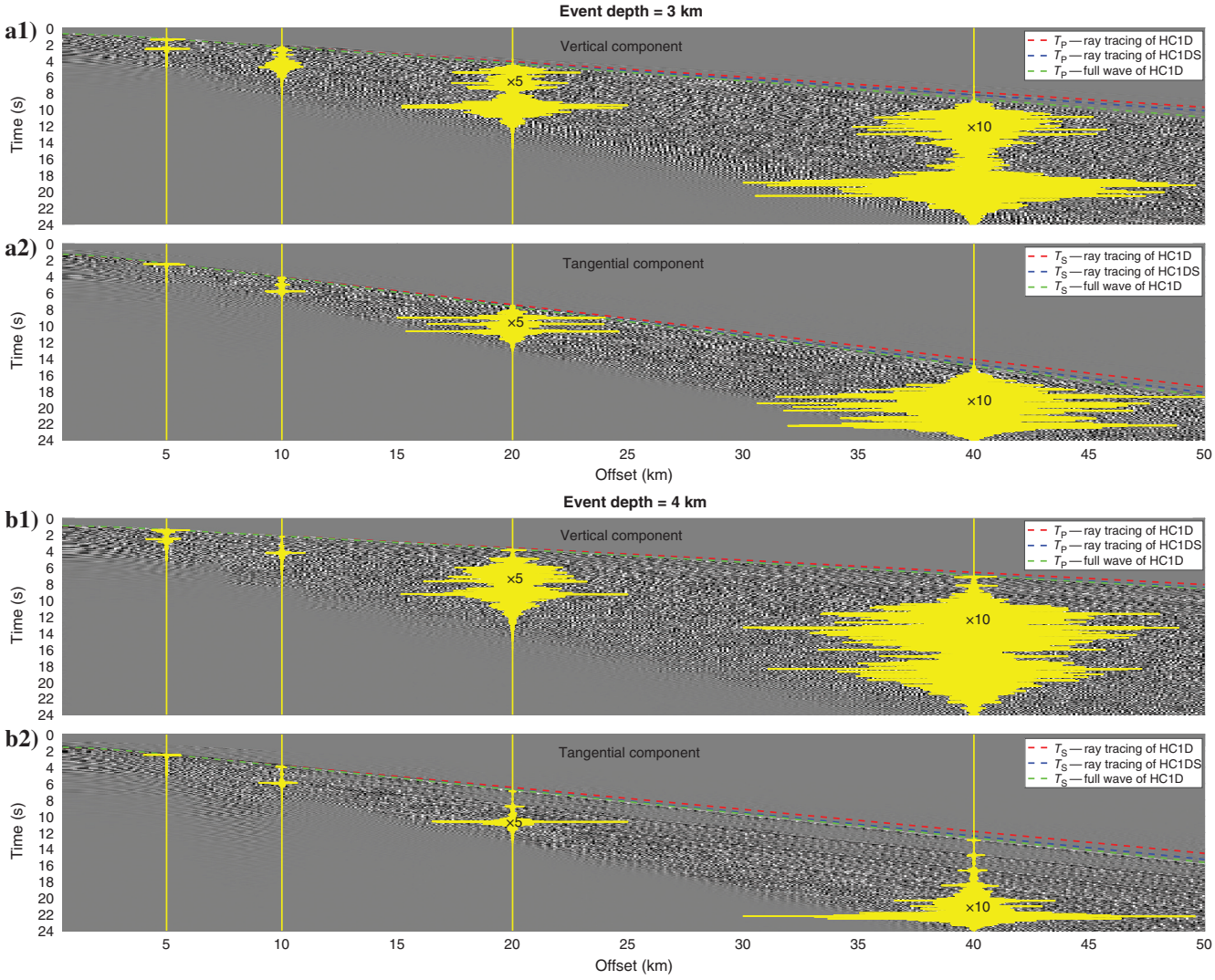


Figure 4. (a1 and a2) and (b1 and b2) Vertical and tangential components of the synthetic wavefield (velocity) excited by double-couple sources at the depth of 3 and 4 km, respectively. The yellow traces show the waveforms at the offsets of 5, 10, 20, and 40 km. The traces at the offsets of 20 and 40 km are, respectively, multiplied by factors of 5 and 10 in plotting. The dashed red and blue curves give the direct waves' (a1 and b1: P wave; a2 and b2: S wave) traveltime calculated from ray tracing of the HC1D and HC1DS models, respectively. The green curves represent the first breaks (a1 and b1: P wave; a2 and b2: S wave) determined from the synthetic full wave data.


DOI:10.1190/geo2023-0238.1

wave traveltime, respectively; $T^{P}_{ref}$ and $t^{P}_{ref}$ are the observed and calculated P-wave traveltime of a selected reference station, respectively; and $N_P$ and $N_S$ are the number of P- and S-wave data, respectively. In equation 1, the differential traveltime $\Delta T^{P}_{n}$ and $\Delta T^{S}_{n}$ represent the P- and S-wave first breaks, respectively (the circles/triangles), shown in Figure 8, whereas $\Delta t^{P}_{n}$ and $\Delta t^{S}_{n}$ are the corresponding modeled templates (the solid/dashed curves). The traveltime reference stations are S1 and S5 for the near and far arrays, respectively.

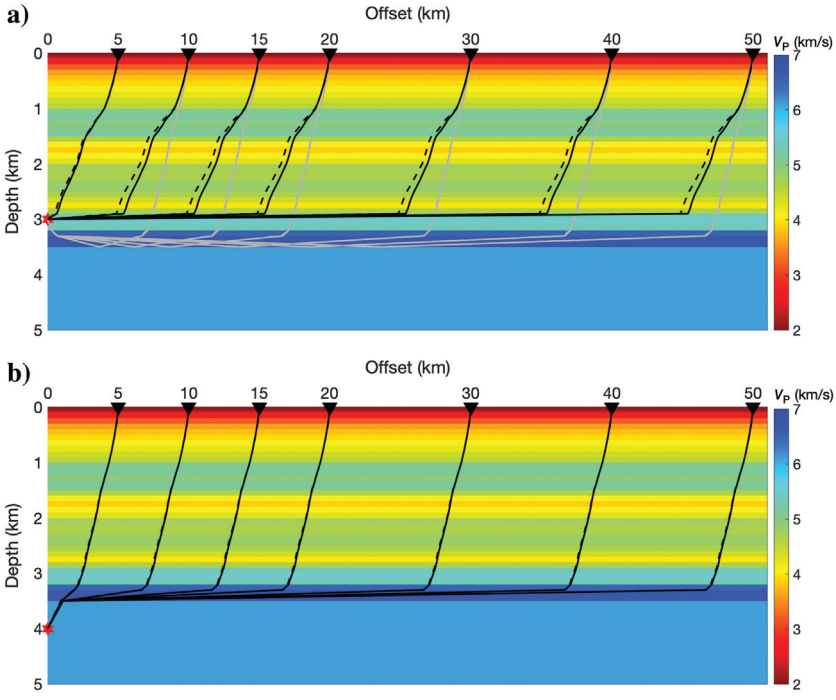


Figure 5. (a and b) The raypaths for the direct P wave (the solid black curves), direct S wave (the dashed black curves), reflected P wave (the solid gray curves), and reflected S wave (the dashed gray curves, which almost overlap with the solid gray curves) in the HC1D model for events located at the depth of 3 and 4 km, respectively. The colored background shows the P-wave velocity of the HC1D model. Note that the reflected waves' raypaths shown in (a) may look like a head wave due to the wide reflection angles at large offsets, but these are not head waves as a head wave is excluded in the ray tracing.

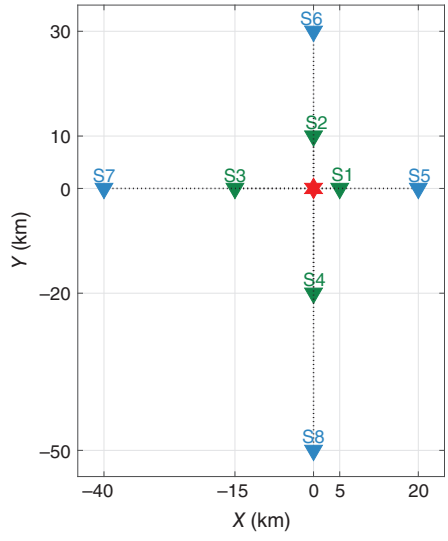


Figure 6. The geometry of the acquisition design that consists of a near-offset array (the green inverted triangles: S1, S2, S3, and S4) and a far-offset array (the blue triangles: S5, S6, S7, and S8). The event is assumed to be located at the origin (the red star).

Figure 9 shows the results of hypocenter inversion using P-wave traveltime data for events at 1–10 km depth. Near and far arrays are examined separately. We first examine the results from the near array, as shown in Figure 9a1–9a4. The HC1DS model has the most accurate epicenter and event depth because it is derived from the HC1D model, which is used to generate the synthetic waveform data. The IASP91 model, as shown in Figure 9a2, provides reasonable estimates for events deeper than 3 km, whereas the DB1D model has a more than 1 km error in event depth but can still give an acceptable epicenter for events in the deep basement. Despite some position errors, all models have traveltime fitting residuals less than 0.13 s (equation 1). In the far array, all three models can provide reasonable estimates of the epicenter for events occurring in the basement, as shown in Figure 9b1, but determining event depth is much more challenging. Due to the finite wavelength effect, the HC1DS model's ray-tracing results at large offsets are invalid, whereas the errors in the ray-tracing templates of IASP91 and DB1D models are greatly amplified at far offsets. As shown in Figure 9b2 and 9b3, the event depths inverted using all three models have large errors. The HC1DS model shows event depths stuck at approximately 3.5 km for events occurring between 4 and 8 km in depth due to the loss of sensitivity below 3.5 km for the traveltime templates (Figure 8b1). This example illustrates that the decrease in inversion sensitivity with large offset data can lead to not only significant inversion uncertainty but also a high risk of systematic bias. The IASP91 and DB1D models overestimate the depth of basement events by several kilometers, as shown in Figure 9b3. This is because the ray tracing of these two models overestimates the P-wave differential traveltime (due to underestimating the seismic propagation velocity) for events in the basement. Consequently, during a grid search, the event position needs to be shifted to a deeper depth to match the waveform's first breaks. Despite the significant deviation of the inverted depths of basement events from the true event depths for IASP91 and DB1D models, their inversion residual in Figure 9b4 is small. This suggests that the inversion traveltime residual is only a metric for evaluating fitting quality but not inversion accuracy.

Figure 10 compares the results of hypocenter inversion using only P-wave traveltime data with those using P- and S-wave traveltime data for events occurring from 1 to 10 km depth, using the HC1DS model. The inclusion of S-wave data helps to constrain event depth, as shown in Figure 10a1 and 10b1, which demonstrates the reduction of overall event depth error for near and far arrays. However, the addition of S-wave data has little impact on the accuracy of the epicenter, as shown in Figure 10a2 and 10b2. This suggests that the accuracy of the epicenter is primarily influenced by the azimuthal coverage of an array and the relative traveltime relationship of the stations.

## Summary of seismic modeling findings

A summary of the findings based on the preceding numerical analyses is as follows:

- The first arrivals of P and S waves exhibit strong and clear signals at short offsets (<10 km), which make the first-break picking process straightforward. However, at large offsets (e.g., >20 km), the first arrivals become dispersive and have weak onset amplitude, leading to significant picking ambiguity.
- Seismic waves propagate laterally along a relatively high-velocity layer around the event depth, leading to a loss of sensitivity of far-offset data to event depth. In addition, the finite wavelength effect causes ray-tracing-based traveltime calculations to become invalid at large offsets. The modeling results shown in Figure 4 indicate that the discrepancies between ray tracing and full wave traveltime can increase from approximately 0.01 to 1 s when the offset changes from 10 to 50 km.
- To obtain reliable hypocenter results, a robust velocity model that represents correctly the local geology (on the scale of the wavelength of seismic waves at frequencies of approximately 10 Hz) and a locally dense array with good azimuthal coverage are equally important.

Note that the validity of ray tracing for traveltime calculations in other areas may vary case by case depending on the actual velocity model. Ray tracing generally works well for models with smooth velocity variations (Červený et al., 2007). The issues with ray tracing addressed in this study are mainly caused by the presence of a high-velocity Ellenburger layer in the Permian Basin, so our findings apply to the Permian Basin or other areas with similar velocity structures.

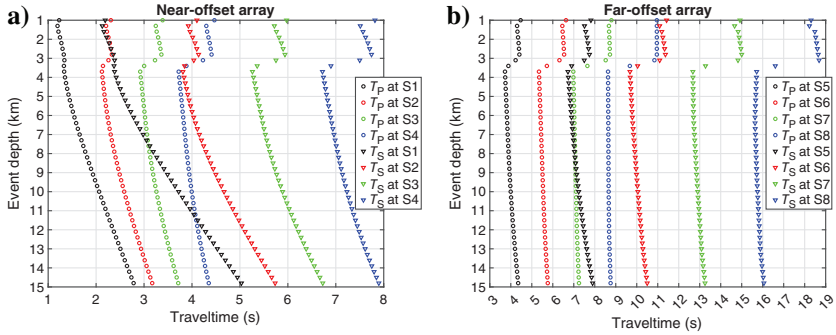


Figure 7. The P- (the circles) and S-wave (the triangles) first breaks derived from the synthetic waveform data of the (a) near and (b) far stations with event depths varying from 1 to 15 km.

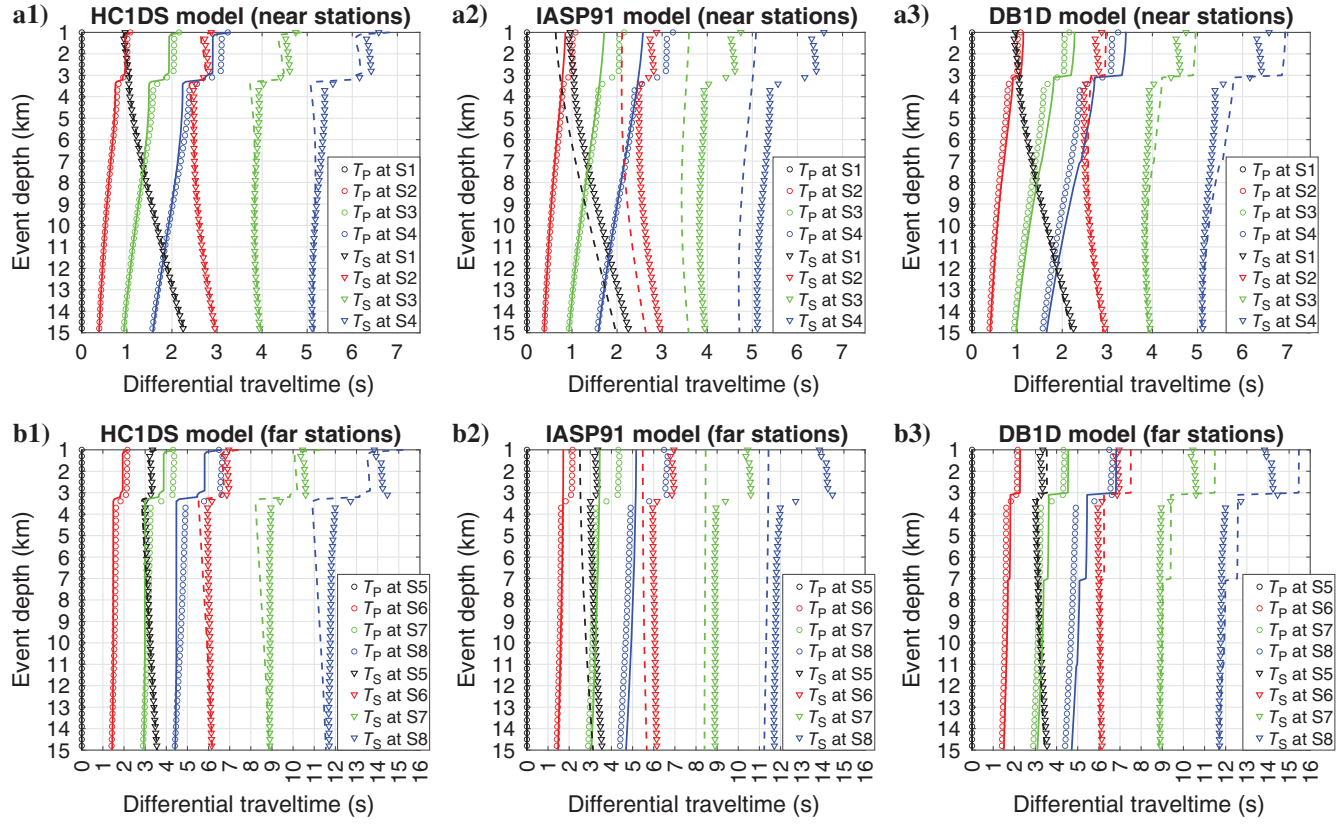


Figure 8. (a1–a3) The P- (the circles) and S-wave (the triangles) first breaks derived from the synthetic waveform data at four near stations with event depths varying from 1 to 15 km together with the ray-traced direct P- (the solid curves) and S-wave (the dashed curves) traveltime. (b1–b3) Similar to the first row except for the far stations. At each event depth, the differential traveltime for near and far stations is defined as the traveltime relative to the P-wave traveltime at stations S1 and S5, respectively.

## REVISITING THE EVENT DEPTHS OF HOWARD COUNTY, TEXAS

Previous modeling studies have provided us with an understanding of the characteristics of the seismic wavefield propagating through the HC1D model as well as the performance of various velocity models in hypocenter inversion. The study in this section focuses on a field data set acquired by a locally dense array consisting of 15 stations located in Howard County, Texas, as shown in Figure 11. All stations are equipped with a 3C seismometer that measures velocity data. Stations 1, 7, 9, and 14 are part of the Texas Network (TexNet), whereas the other stations belong to a privately deployed array in Howard County. For this study, we select three TexNet reported events (represented as red stars in Figure 11 and provided in Table 2) that are surrounded by these 15 stations. This presents an opportunity to examine the impact of station-to-event distance (i.e., offset) on hypocenter inversion. Based on their distance from the events, we divide these 15 stations into three groups. The first group, called the "near subarray," comprises stations 1–6 (the green triangles), whose offsets to the three selected events are within 20 km. The second group, known as the "far subarray," consists of stations 10–15 (the blue triangles), whose distances from

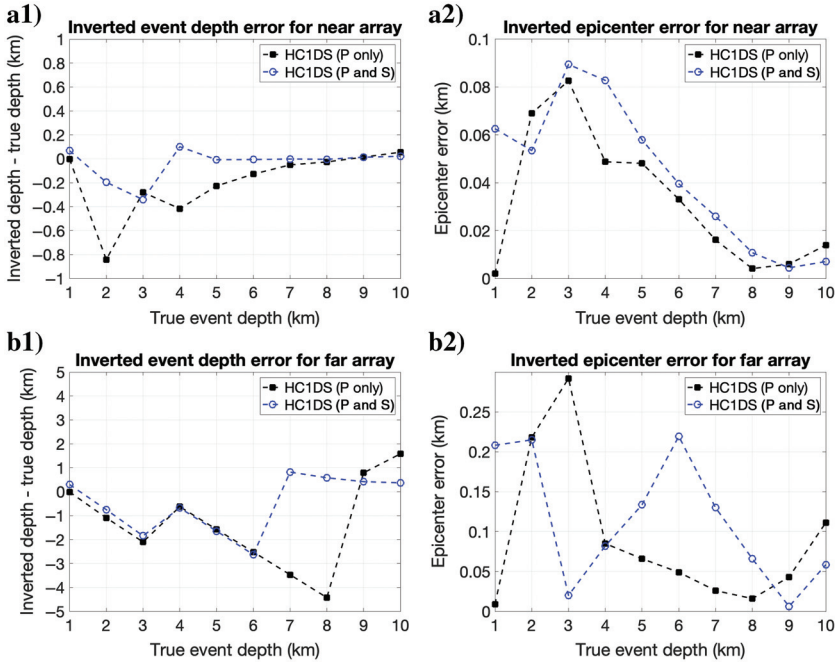


Figure 10. Comparisons of the hypocenter results inverted from the data with (the blue circles) and without (the black squares) S-wave first-break data using the HC1DS model.

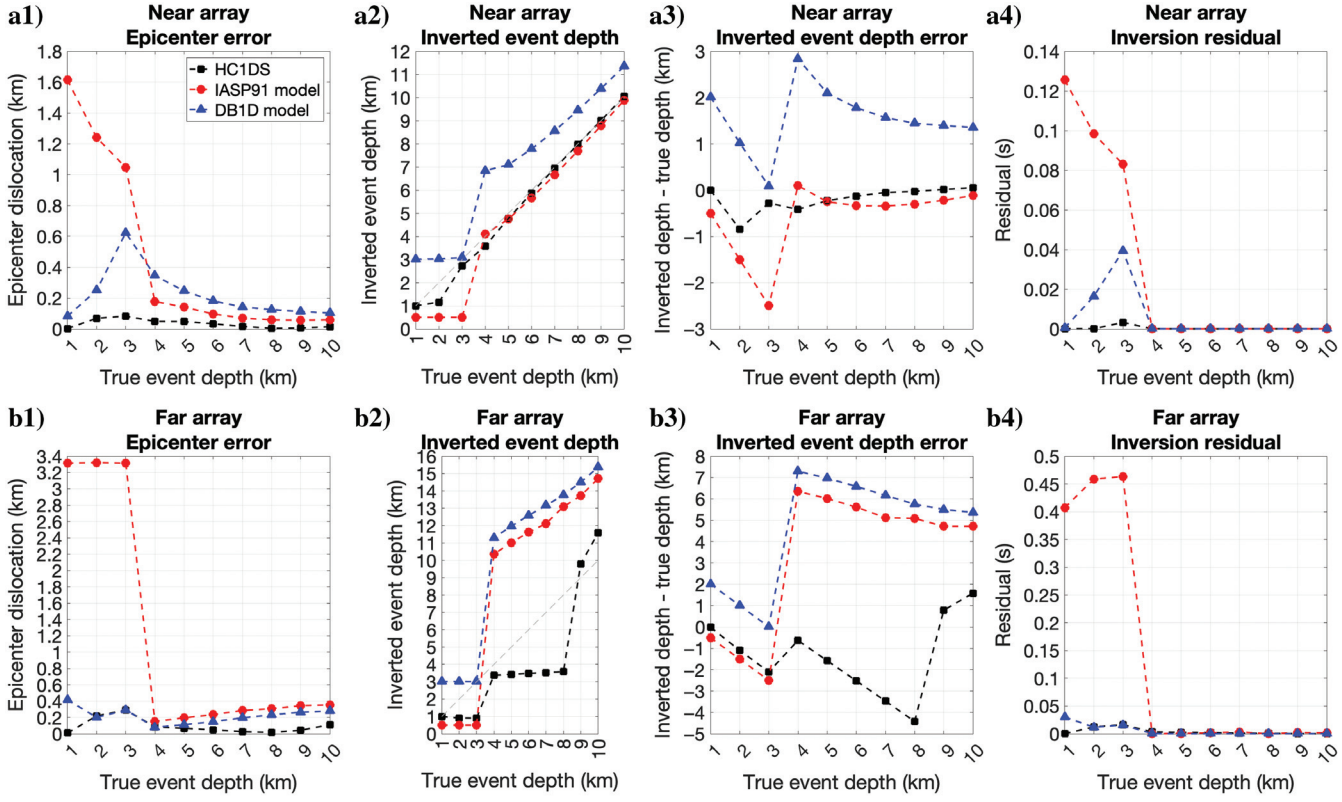


Figure 9. (a1–a4) and (b1–b4) The event hypocenter inversion results using the P-wave first-break data of the near array (S1, S2, S3, and S4) and the far array (S5, S6, S7, and S8), respectively.

DOI:10.1190/geo2023-0238.1

the events vary from approximately 30 to 40 km. The remaining three stations (the black triangles) belong to the last group, which serves as a transition between the near and far subarrays.

## Preprocessing and inversion setup

During the preprocessing, we apply a 2.5–25 Hz band-pass filter to the raw waveform data to enhance the signal-to-noise ratio (S/N). In Figure 12, we plot the manually picked P-wave first breaks (the vertical red bars) and S-wave first breaks (the vertical green bars) on the 3C velocity data of the three events. Note that we do not perform picking for the data of station 15 for event 2 and station 9 for event 3 due to poor data quality. It is worth pointing out that picking the P- and S-wave first breaks for far stations requires a very careful and time-consuming trace-by-trace examination. This is due to the weaker amplitude of P waves for far stations compared with that for near stations, and the S-wave first arrivals being susceptible to being masked by other signals, such as layer reverberations and P-wave codas.

We compare the following six data scenarios for each event to understand how the wave type (P and S versus P only) and station distance (near versus far) influence the inversion of event hypocenters:

- P- and S-wave first breaks from near subarray,
- P- and S-wave first breaks from far subarray,
- P- and S-wave first breaks from all stations,
- P-wave first breaks from near subarray,
- P-wave first breaks from far subarray, and
- P-wave first breaks from all stations.

We compare P- and S-wave first breaks with P-wave first breaks only because it can be challenging to reliably pick S-wave first breaks in many circumstances, and the P-wave first arrivals are given greater weight in the inversion process. Our aim is to understand if there are significant changes in the inversion results when using P- and S-wave first breaks compared with using only P-wave first breaks. We conduct three separate inversions for each data scenario using HC1D, IASP91, and DB1D models (Figure 3). For the HC1D model, we generate P- and S-wave traveltime templates based on the first breaks obtained from synthetic full wave waveforms to eliminate the finite wavelength effect. The P- and S-wave traveltime templates for the IASP91 and DB1D models are generated through ray tracing.

## Comparisons of hypocenter inversion results

We use a grid search approach to minimize the objective function of equation 1 and obtain the optimal epicenter and event depth for each event. We then compare the results obtained from different combinations of data wave type (P and S first breaks versus only P first breaks), station offset (near subarray, far subarray, and all stations), and three velocity models (HC1D, IASP91, and DB1D). After estimating the event hypocenter, we calculate the P- and S-wave first-arrival times using the estimated hypocenter with waveform modeling. We then use these modeled arrival times to align all traces for quality control (QC). In the ideal scenario in which the modeled P- and S-wave first-arrival times exactly match the picked data, all traces should perfectly align at time zero. This visualization provides an intuitive way to perform inversion QC and verify the accuracy of the inverted event location. In addition, when only a subset of the data, such as the near subarray or far subarray, is used in the inversion process, evaluating the alignment of the complementary data that are not used in the inversion provides good QC metrics for assessing the reliability of the inversion.

Figure 13 shows a comparison of aligned waveforms for event 1, using the hypocenters inverted from the HC1D model. Figure 13a1–13a3 and 13b1–13b3 and Figure 13c1–13c3 and 13d1–13d3 shows the results inverted using P- and S-wave data and P-wave data only, respectively. Within each panel, the first row displays the aligned vertical component waveforms for the event hypocenter inverted using the near subarray (Figure 13a1, 13b1, 13c1, and 13d1), far subarray (Figure 13a2, 13b2, 13c2, and 13d2), and all stations (Figure 13a3, 13b3, 13c3, and 13d3), respectively. The second row

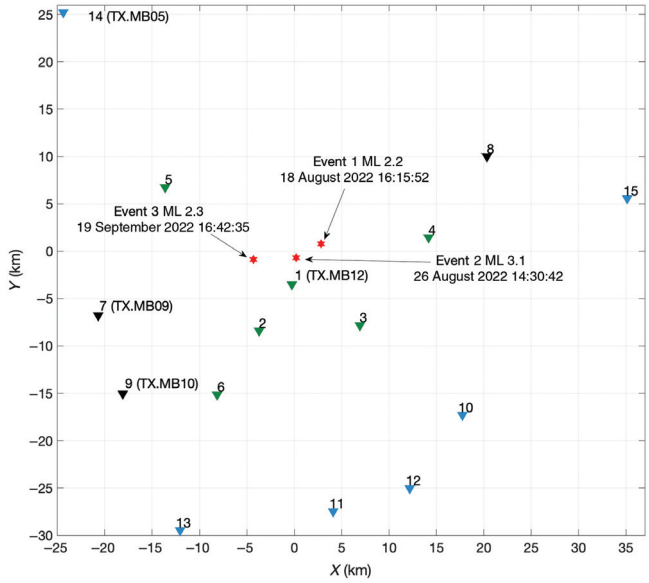


Figure 11. Locations of the 15 stations that comprise the Howard County local array and the positions of the three selected events (the red stars) reported by TexNet (see Table 2). Green and blue triangles represent the near and far subarrays' stations, respectively, and the black triangles correspond to the transition stations between the near and far subarrays.

**Table 2. Parameters of three selected induced seismic events reported by TexNet (TexNet, 2023).**

| | Event 1 | Event 2 | Event 3 |
|---|---|---|---|
| Event ID | texnet2022qdqk | texnet2022qscz | texnet2022skdj |
| Origin time (UTC) | 18 August 2022 16:15:52 | 26 August 2022 14:30:42 | 19 September 2022 16:42:35 |
| Latitude (°) | 32.407 | 32.394 | 32.392 |
| Longitude (°) | −101.570 | −101.598 | −101.646 |
| Depth, relative to the surface (km) | 7.7 (±1.5) | 12.2 (±1.2) | 8.1 (±1.3) |
| Local magnitude (ML) | 2.2 | 3.1 | 2.3 |

shows the aligned horizontal component waveforms. Let us first discuss the results inverted using P- and S-wave data. When the near subarray is used for event hypocenter inversion and the far subarray is used only for inversion result QC, as shown in the left column of Figure 13, excellent alignment of the shifted P-wave waveforms suggests that the inverted hypocenter position is consistent with the P-wave data recorded at all stations and the P-wave velocity model used for traveltime calculation. Furthermore, consistent alignment across the near and far subarrays indicates that the inversion is robust and stable. Some misalignments of the shifted S-wave waveforms from the far subarray data are observed, which can be caused by various factors, such as formation anisotropy effect (e.g., shear splitting), wave-mode conversion (e.g., P-to-S converted waves), and formation lateral variations and heterogeneities. When the far subarray is used for event hypocenter inversion and the near subarray is used only for inversion result QC, the alignment of shifted P- and S-wave waveforms (Figure 13a2 and 13b2) is considerably worse when compared with the near subarray's inversion. When using all stations for event hypocenter inversion, the alignment of shifted P- and S-wave waveforms (Figure 13a3 and 13b3) improves from the far subarray scenario but is still not as good as the near subarray scenario. This could be because the local velocity model used in the inversion may be accurate within 20 km, but beyond that distance, the wave propagation time may not be properly accounted for with a 1D model. A 3D velocity model may be necessary to accurately model wave propagation at distances beyond 20 km. Full wave modeling is required as ray tracing is no longer a valid method for calculating traveltimes beyond 10 km. However, constructing traveltime templates using numerical modeling tools such as finite difference for a 3D velocity model at a county-wide scale requires tremendous computational power, not to mention that building such an accurate 3D velocity model itself is nontrivial. These challenges make it difficult to use far subarray data for accurately estimating event hypocenters.

Figure 13c1–13c3 and 13d1–13d3 shows comparisons of the waveforms shifted based on the results inverted from the P-wave data only. The alignment of the waveforms for the case of the near subarray shown in Figure 13c1 and 13d1 is as good as those in Figure 13a1 and 13b1, which suggests that using S-wave first breaks from the near subarray is helpful but not essential for obtaining good results. The alignment of P and S waveforms inverted using all stations' P-wave data (Figure 13c3 and 13d3) is reasonable. In the case of the far subarray (Figure 13c2 and 13d2), the alignment of the shifted P-wave waveforms from the far subarray is good, which suggests that our inversion algorithm works satisfactorily. The waveforms for the near subarray's P waves and all stations' S waves show very poor alignment. This could be partially attributed to the limited sensitivity of the far stations' P-wave data to event depth. In addition, a local 1D velocity model may be insufficient for the calculation of wave propagation traveltime at long distances.

Figure 14 compares the alignment of waveforms for the results of event 2 inverted using the HC1D model. In the case of using P- and S-wave data (Figure 14a1–14a3 and 14b1–14b3), the first-break picks and traveltimes modeled using the HC1D model show a level of agreement similar to those for event 1. However, when using P-wave data alone (Figure 14c1–14c3 and 14d1–14d3), only the inversion with the near subarray data yields reasonable results for event 2, whereas the far subarray and all stations' inversions result in poorly aligned waveforms. Figure 15 shows comparisons of the waveform alignment for event 3 results. As observed for event 2, the inversions with near subarray data produce consistent and reliable results, regardless of whether S-wave data are included or not. However, for far subarray data, even with the inclusion of S-wave data, the inversions are unstable.

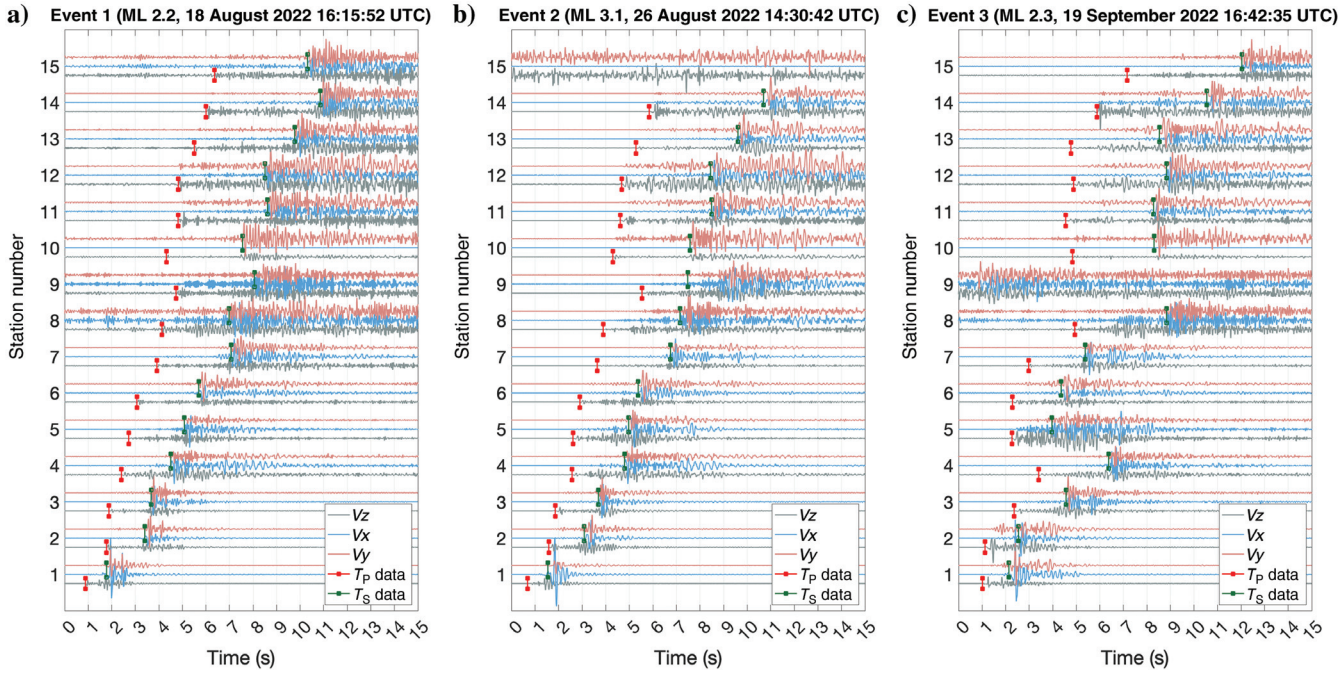


Figure 12. The 3C waveforms for the three events provided in Table 2. Black, blue, and red traces correspond to the vertical, north, and east components, respectively. Vertical red and green bars, respectively, mark the manually picked P- and S-wave first breaks. The waveforms of each station are self-normalized in plotting.

The comparisons of inversion results using IASP91 and DB1D models are presented in Appendices A and B. Compared with the HC1D model, the other two models have poorer performance in terms of waveform data alignment. The results obtained from these three models exhibit a pattern whereby inversions that use data from near stations (such as near subarray or all stations) tend to yield consistent and reasonable results. Conversely, inversions that only use far subarray's data are not reliable, even with the inclusion of S-wave data.

## Epicenter uncertainty analysis

In this section, we analyze epicenter uncertainty for the events using a bootstrapping approach, which recursively runs inversion on a subset of the data to estimate the variations. Figures 16, 17, and 18 show the epicenters obtained through inversion using various data scenarios and velocity models, and the back azimuth ranges of these three events estimated from the TexNet station MB12s P-wave polarization. For event 1, the epicenters inverted from the near subarray and all stations (the squares and triangles) cluster closely together and fall within the back azimuth range. In contrast, the epicenters inverted from the far subarray (the circles) have large uncertainties and fall outside the back azimuth range. TexNet reported epicenter (the cyan star) is located several kilometers away from our results and falls outside the back azimuth range. Furthermore, the results obtained using the IASP91 model (in red) and the DB1D model (in blue) exhibit greater uncertainties than those obtained using the HC1D model (in black). For events 2 and 3, the HC1D model yields significantly less uncertainty in the inverted epicenter results compared with the IASP91 and DB1D models. Notably, TexNet reported epicenters and our inverted results fall within the estimated back azimuth ranges, except for a few instances where P-wave data alone are used (see Figures 17b and 18b). In summary, the inverted epicenters for all three events exhibit a trend that epicenters inverted from the same data set but different velocity models (i.e., symbols of the same shape but with different colors) tend to cluster together, indicating that acquisition geometry has a bigger impact on the epicenter inversion than the velocity model. This observation is consistent with what we saw in the previous numerical modeling section.

## Event depth analysis

In this section, we compare the event depths obtained from our inversions and those reported by TexNet. Note that TexNet uses the IASP91 model for event location in the Howard County area according to the report of Savvaidis et al. (2019). Figure 19 shows the inverted depths of all three events using different velocity models and data sets, as well as the depths reported by TexNet

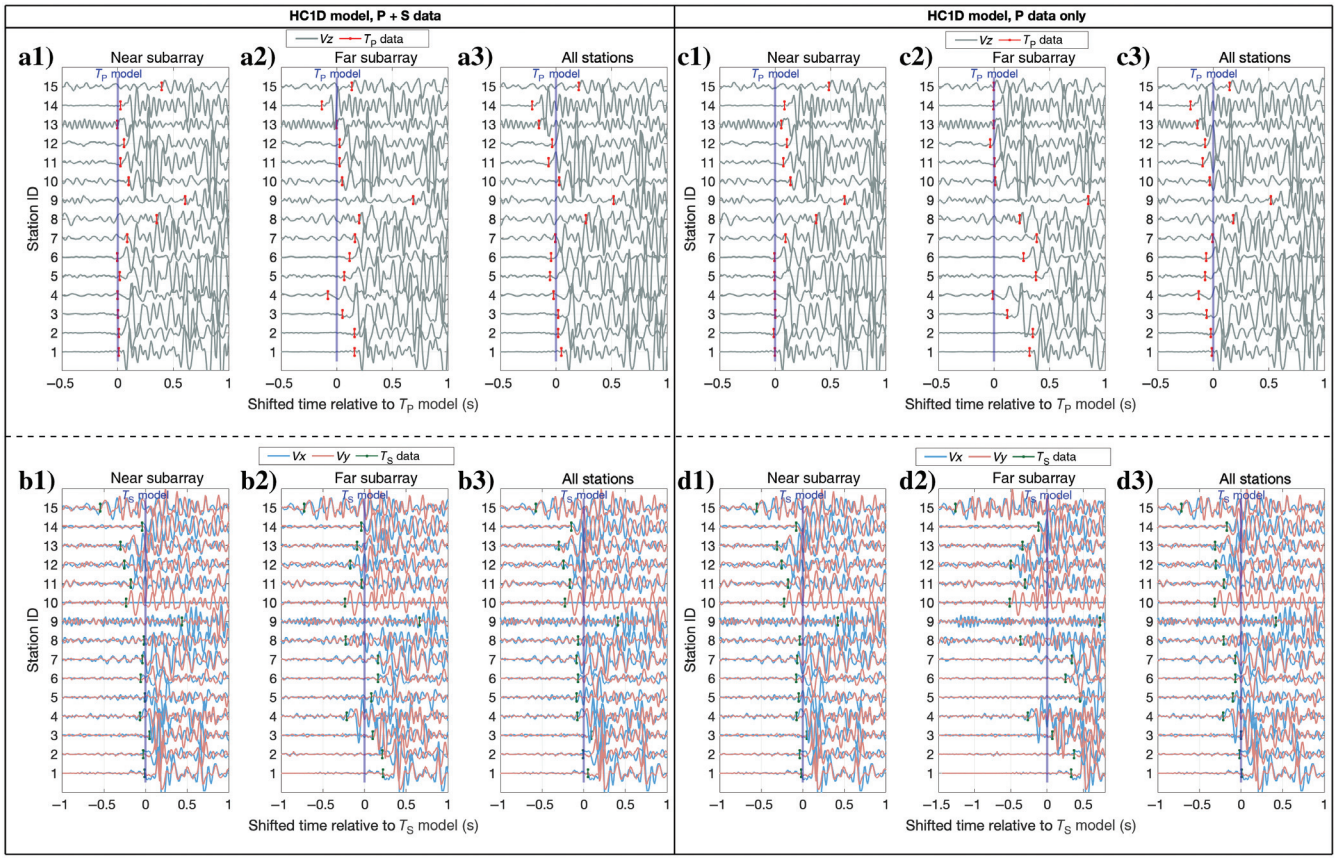


Figure 13. (a1–a3 and b1–b3) and (c1–c3 and d1–d3) The results for event 1 inverted using P- and S-wave data and P-wave data only, respectively. In each panel, the first and second rows, respectively, show the vertical and horizontal components' waveforms with each trace's time zero shifted to the corresponding station's P-/S-wave modeled arrival times, which are calculated based on the hypocenters inverted from the data of near subarray, far subarray, and all stations using the HC1D model. The vertical red and green bars, respectively, show the P- and S-wave first breaks picked from the data.

(shown with the dashed red lines). Notably, for most scenarios, the depths inverted from the HC1D model are much shallower than TexNet values, except for those using the far subarray's P-wave data (represented by the empty circles). As discussed in the "Seismic modeling study" section, far stations' data have very limited sensitivity to event depth, so a minor picking error in the data can cause a significant drift in event depth. Although S-wave data can help somewhat constrain event depth for far stations, it does not improve epicenter accuracy, as shown in Figure 16a. Meanwhile, accurately picking S-wave first breaks from far stations demands careful scrutiny of each trace and can be a laborious and time-consuming process. This makes it infeasible to manually process large amounts of data. Although automated picking algorithms based on artificial intelligence or machine learning (ML) could potentially aid in S-wave first-break picking, there are instances where even human experts may struggle to accurately identify S-wave first breaks, raising concerns over the reliability of such algorithms for picking from far-offset data. In contrast, S-wave first breaks recorded by near stations can be easily identified and picked using automated picking algorithms. The event depths inverted with the IASP91 and DB1D models using different data scenarios exhibit large variations, suggesting that these models are inconsistent with the observed data. When using data from the far subarray in the inversions, the inverted event depths from the DB1D model tend to approach the depths reported by TexNet. We conduct an additional validity check for the event depth results using the time difference between the S- and P-wave first breaks (i.e., $T^S - T^P$) at the TexNet station MB12, which has the best S/N as it is only a few kilometers away from the events. The $T^S - T^P$ time at a single station provides a constraint on the maximum allowed event depth (calculated using HC1D), as the event cannot be deeper than the depth corresponding to the $T^S - T^P$ time from a hypothetical source located directly beneath the station (Sheng et al., 2022). Interestingly, TexNet reported depths for all three events (the solid circles) exceed the maximum allowed event depth of the individual events (the dashed lines) and the depths for events 1 and 2 are not possible even after taking the depth uncertainty (reported by TexNet) into account, as shown in Figure 20, indicating that the reported depths are not plausible. In contrast, the depth results obtained from the near subarray's P- and S-wave data using the HC1D model fall within a narrow depth range of 3.5–3.6 km for all three events (see Table 3), suggesting that these events occurred near the top of the basement (see Figure 3b) rather than in the deep basement, as reported by TexNet. This discovery could result in a different understanding of the triggering mechanism for induced seismicity in the area as well as significant differences in estimated event magnitudes. We use the model of Kavoura et al. (2020), which is the ML model used by TexNet, to recalculate the ML based on our inverted event hypocenter. Our calculations, as shown in Table 4, give smaller ML values for all three events compared with those reported by TexNet, due to our shallower inverted event depths. This implies that the reported ML values of the events in the Permian Basin could be overestimated due to incorrect event depths.

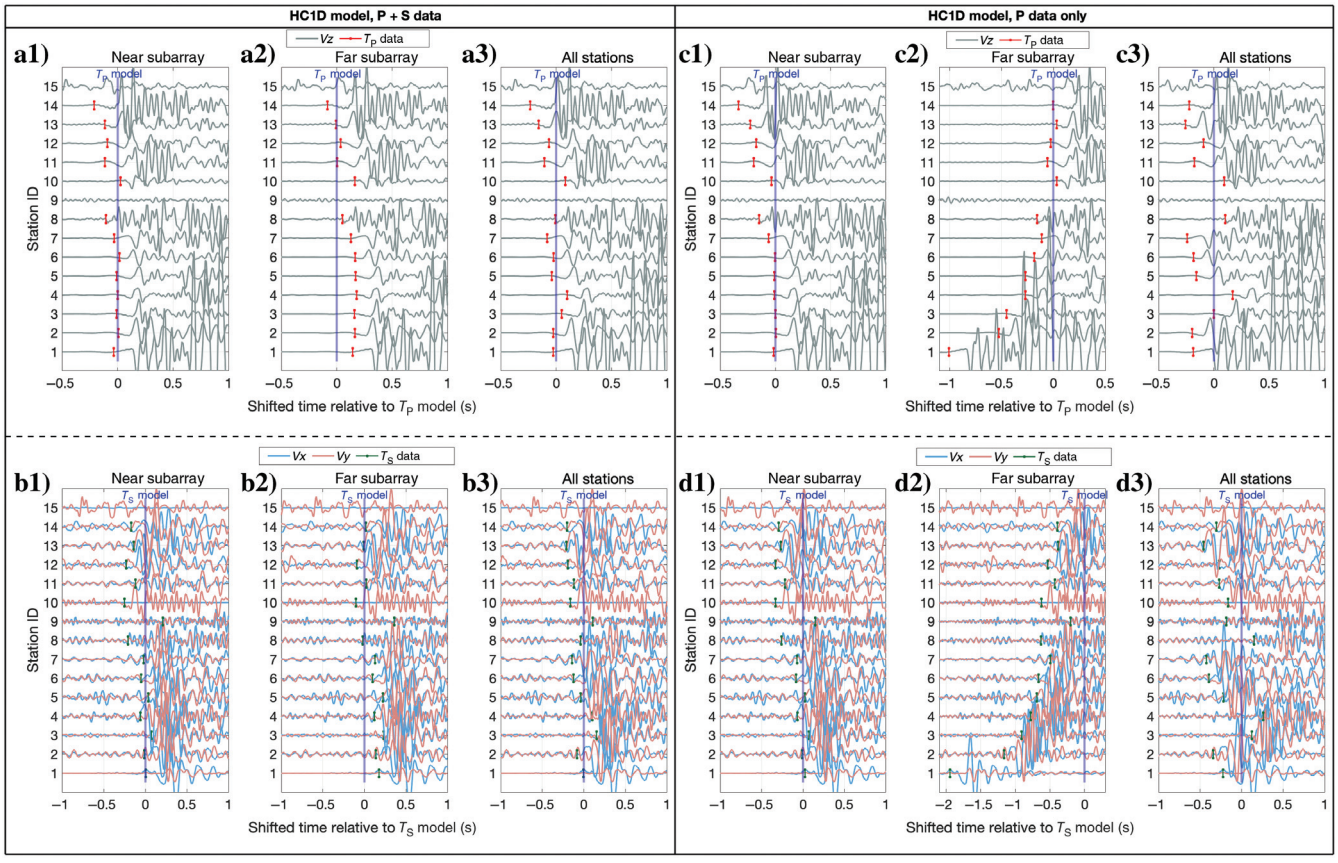


Figure 14. Similar to Figure 13, for comparisons of event 2 results inverted using the HC1D model.

## DISCUSSION

From the modeling studies and field case analyses, we have determined that monitoring induced seismic events using distant stations (with offsets greater than 10 km) present the following challenges:

- Accurate event location requires a robust sedimentary layered velocity model that honors the actual formation P- and S-wave velocities. Crustal velocity models that are designed for far field and teleseismic events are not appropriate for local earthquakes that travel mostly through the sediment section instead of long paths through the basement rocks.
- Seismic waves generated by local shallow earthquakes and recorded at distant stations involve a significant horizontal travel path, resulting in the propagation velocity being primarily associated with the formation's horizontal velocity. However, velocity models used in event hypocenter inversion are typically constructed based on sonic logs or VSP data, which mainly measure the vertical velocities of

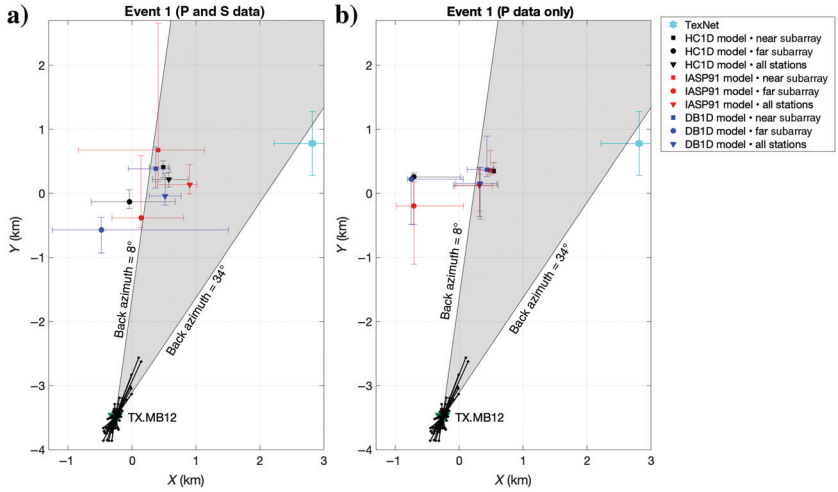


Figure 16. Epicenters inverted from different combinations of data scenarios (the squares: near subarray; the circles: far subarray; the triangles: all stations; [a] inversion with P and S data and [b] inversion with P data only) and velocity models (the black: the HC1D model; the red: the IASP91 model; and the blue: the DB1D model). The cyan stars represent the event positions reported by TexNet and the associated error bars indicate the reported epicenter uncertainty. The gray shaded areas represent the ranges of back azimuth estimated from the station TX.MB12's P-wave horizontal polarization (the black rays). The error bars (the solid lines) for each symbol represent the uncertainty estimated through bootstrapping.

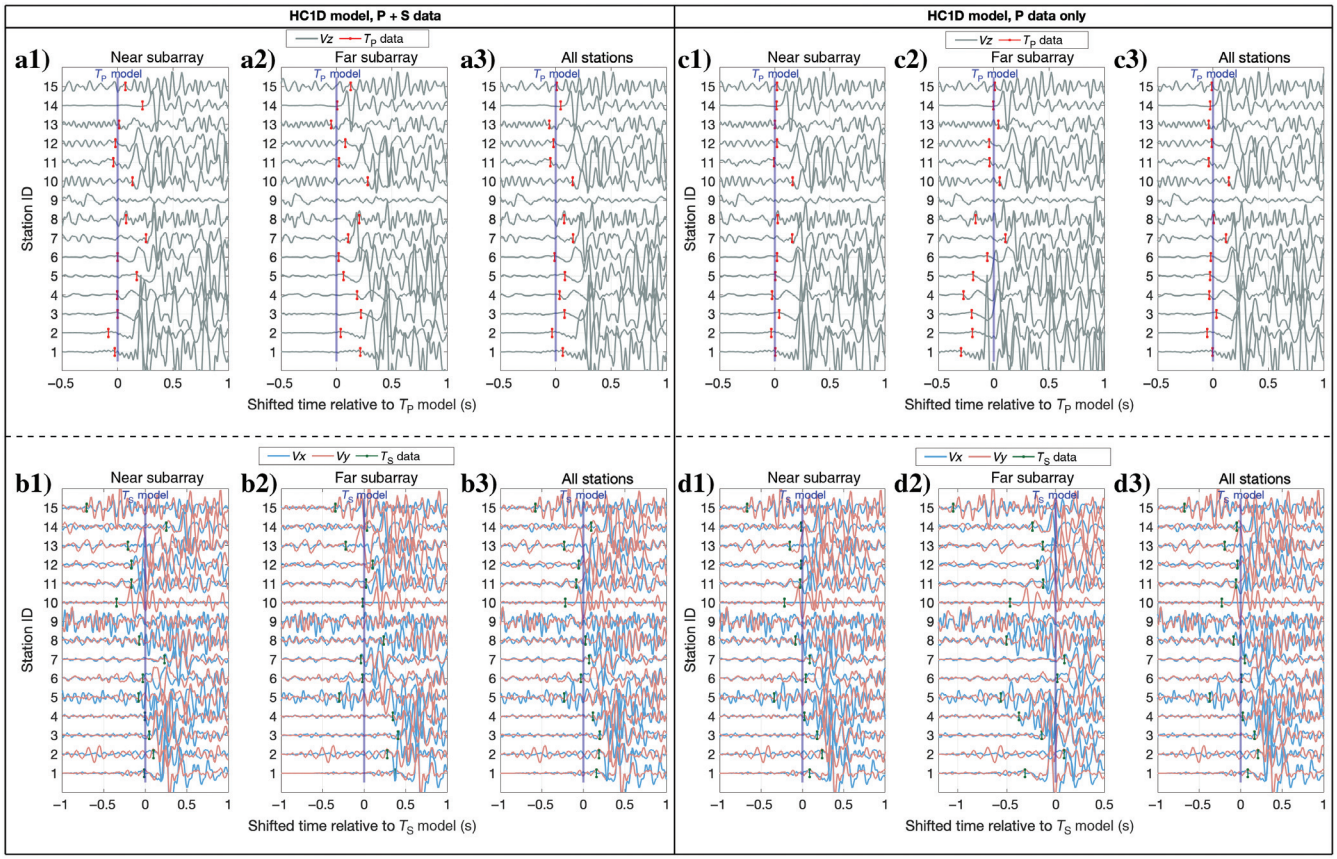


Figure 15. Similar to Figure 13, for comparisons of event 3 results inverted using the HC1D model.

formations. Sedimentary formations with lateral laminations often exhibit vertically transverse isotropic (VTI) anisotropy, which causes horizontal velocity to be faster than vertical velocity. Although seismic full wave modeling using a fine layer model (e.g., sonic log scale) with layer thicknesses much smaller than the seismic wavelength can effectively simulate the anisotropy induced by formation lamination, the influence of intrinsic anisotropy present in formations such as shale is still difficult to be taken into account as this type of anisotropy cannot be directly obtained from conventional logging data. As a result, a velocity model constructed based on sonic logs or VSP data may underestimate the seismic wave's propagation velocity for far field events when VTI anisotropy is present. The underestimation in propagation velocity would lead to overprediction of differential traveltime between stations and increasing fitting residuals, which is compensated through shifting the hypocenter to a deeper depth (equivalent to reducing the wave paths' difference between stations) in the inversion. Thus, the underestimation of seismic velocity could result in an overestimation of event depth, as demonstrated by the results of the IASP91 and DB1D models shown in Figure 9b2. In addition, when a high-velocity layer with a thickness less than or close to the dominant seismic wavelength is present, the tunneling effect caused by the high-velocity layer could invalidate conventional ray-based traveltime calculation methods, which are commonly used for event hypocenter inversion.

- Traveltime data recorded at distant stations have little sensitivity to event depth, resulting in depth uncertainty on the order of kilometers. Furthermore, the drop in sensitivity also increases the inversion's susceptibility to noise and picking errors. The modeling study illustrated in Figure 9b2 shows that even a small picking error can overwhelm the inversion and cause a drift of several kilometers in event depth. The inclusion of S-wave data from distant stations may or may not resolve this issue, as S-wave data's sensitivity also decreases at large offsets, and S-wave first breaks have larger picking ambiguities at large offsets compared with near offsets. Because S-wave velocity models and first-break picking are generally less reliable than P wave, we need to comprehensively evaluate the risks and benefits of using far stations' S-wave data and then make a trade-off in our practices. This also requires the consideration of more sophisticated approaches using 3D VTI models to improve the results.
- The synthetic waveform data and the field data demonstrate that picking P- and S-wave first breaks at large offsets can have significant uncertainty because they become dispersive at long distances and do not have clear first breaks. Note that although we perform elastic modeling by assigning a constant high $Q$ value of 2000 to the entire model in this study, shallow events propagating at long distances in field situations inherently suffer from more complex attenuation effects from a variable $Q$ in different sedimentary rocks along with anisotropy, mode conversions, and other complex wave phenomena. Given the decrease in distant stations' data sensitivity to event depth, incorrect first-break picking can result in hypocenter mislocation of several kilometers.

The limitations of ray tracing due to high-velocity contrast and fine layering, as well as the problem of first-break picking, can be addressed by using wave-based hypocenter location methods (Li et al., 2020). These methods locate hypocenters using an imaging-like approach through

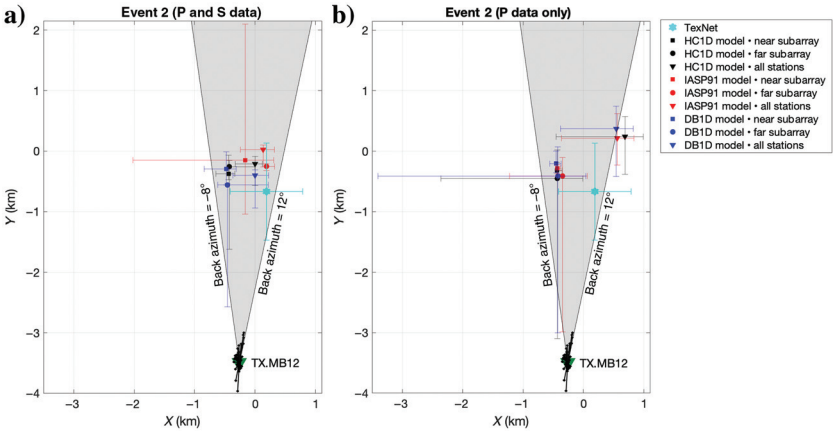


Figure 17. (a–b) Similar to Figure 16a and 16b, respectively, for event 2.

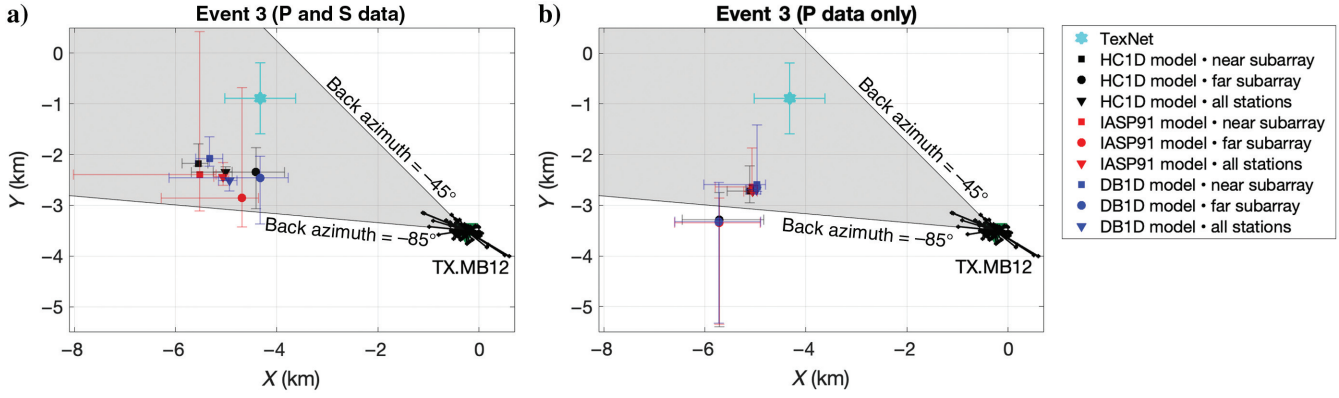


Figure 18. (a–b) Similar to Figure 16a and 16b, respectively, for event 3.

wavefield back propagation. However, the low data sensitivity issue at large offsets would still make the wave-based methods susceptible to velocity model inaccuracy. In addition, the velocity model used for back propagation must correctly account for the vertical and horizontal velocities of formations (i.e., VTI anisotropy) to accurately locate near and far events. When the lateral velocity variations of the formations between stations and event locations exceed a certain limit, the 1D model assumption will break down and become invalid, and hypocenter inversion requires an anisotropic 3D model. However, implementing a 3D model in practice is often not feasible due to the limitations of data availability and computational efficiency. The most practical solution to overcome these challenges is to deploy a local array.

Based on the numerical modeling results shown in Figure 4, we can see that complex velocity structures in sedimentary basins can create complex mode-converted waves and surface reverberations. Regional crustal models, such as the IASP91 and DB1D, which do not consider the basin architecture and local velocity structures,

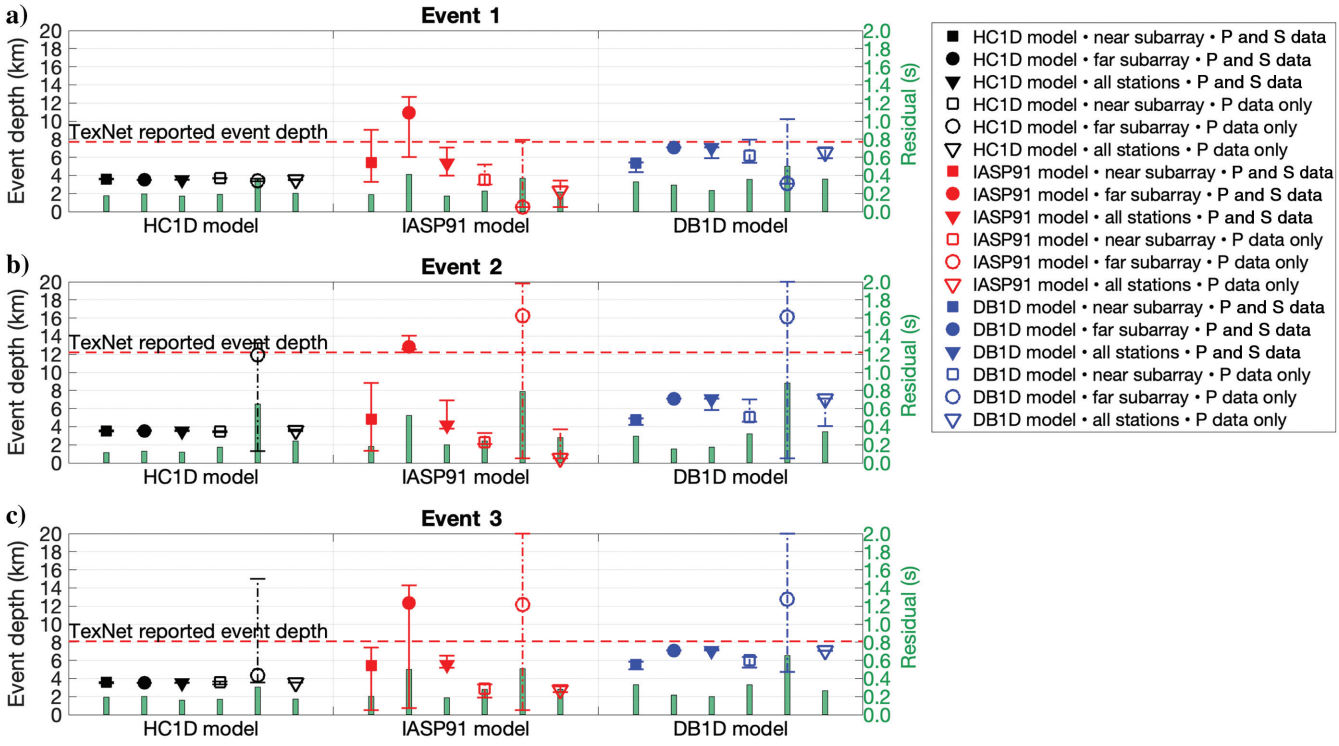


Figure 19. Event depth inverted from different combinations of data scenarios. The symbols' definitions are similar to those in Figure 16 except that the results inverted from P-wave data only are represented by open symbols. The dashed red lines indicate the event depth reported by TexNet (Table 2). The error bars (the dashed-dotted lines: P data; the solid lines: P and S data) for each symbol represent the uncertainty estimated through bootstrapping. The histograms in green represent the inversion residual. Note that station 9 is excluded from the residual calculation because of its data inconsistency.

**Table 3. Comparisons of event depths inverted from different velocity models.**

| | | P and S | | | P | | |
|---|---|---|---|---|---|---|---|
| Velocity model | Event | Near subarray (m) | Far subarray (m) | All stations (m) | Near subarray (m) | Far subarray (m) | All stations (m) |
| HC1D | 1 | 3600 | 3500 | 3500 | 3682 | 3385 | 3532 |
| | 2 | 3545 | 3508 | 3539 | 3469 | 11,920 | 3588 |
| | 3 | 3576 | 3500 | 3519 | 3554 | 4322 | 3547 |
| IASP91 | 1 | 5433 | 10,932 | 5360 | 3521 | 500 | 2305 |
| | 2 | 4840 | 12,783 | 4180 | 2296 | 16,220 | 500 |
| | 3 | 5385 | 12,317 | 5530 | 2897 | 12,150 | 2755 |
| DB1D | 1 | 5367 | 7100 | 7100 | 6188 | 3081 | 6537 |
| | 2 | 4757 | 7100 | 7100 | 5045 | 16,120 | 7100 |
| | 3 | 5517 | 7100 | 7100 | 6020 | 12,779 | 7058 |


DOI:10.1190/geo2023-0238.1

fail to model the raypath distortions caused by complex modes of wave propagation, resulting in inaccurate estimation of event locations. Thus, relying on deep earth crustal velocity models to locate events in a sedimentary basin is fundamentally flawed and should be avoided. Errors in the depths of seismic events lead to errors in event magnitude that must be corrected as events are relocated with more reliable local models (e.g., HC1D). Moreover, unreliable event locations and magnitudes would lead to incorrect earthquake causation analysis and inhibit the planning of effective mitigation strategies for induced seismicity.

Note that our findings regarding the performance of different array configurations and problems with ray tracing in hypocenter inversion are based on the study of the induced seismicity in the Permian Basin. This study can provide some guidance on induced seismic monitoring in areas with similar velocity structures, but the relative contributions of various factors, such as the velocity model, seismic modeling method, and array configuration, in hypocenter inversion need to be analyzed specifically for a given area.

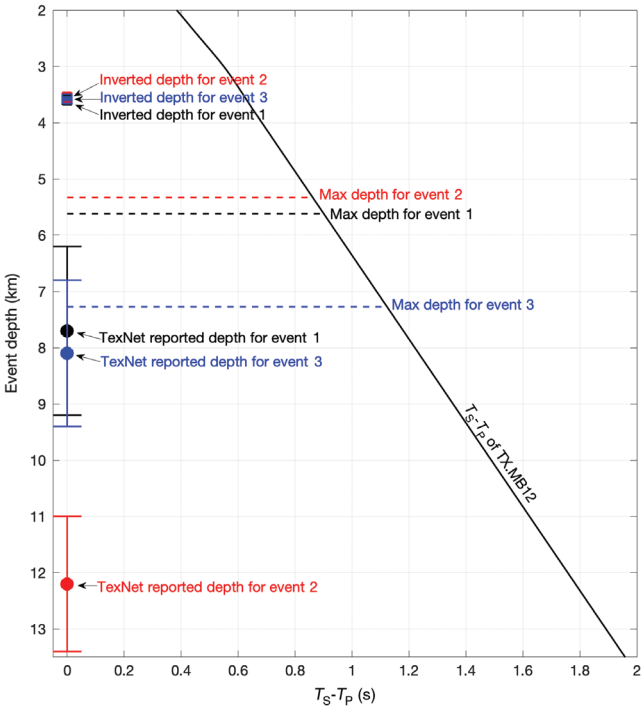


Figure 20. Comparisons of the event depths inverted from the near subarray's P- and S-wave data (the squares) and those reported by TexNet (the circles with error bars representing uncertainty) as well as the maximum allowed event depths (the dashed lines) constrained by the S- and P-wave first-break difference at the TX.MB12 station. The solid black curve gives the S- and P-wave zero-offset traveltime difference calculated using the HC1D model.

## CONCLUSION

Our numerical modeling and field data analyses indicate that the use of regional crustal models that fail to account for basin architecture and local velocity structures, coupled with the insensitivity of large offset arrays to event depth and large picking uncertainty caused by weak and complicated P- and S-wave arrivals, can result in unrealistic event depths and very large uncertainties in event epicenters in the Permian Basin. Improvements in processing alone are insufficient to overcome these issues. Given the challenges mentioned previously, a practical approach to obtaining reliable hypocenters of induced events is to use regional seismic arrays to identify the onset of seismic activity and then deploy a local dense monitoring array (station spacing should be <10 km) with an accurate local velocity model for robust event locations and seismic causation analysis. Data recorded at close stations have a high S/N, high sensitivity to hypocenter position, and low sensitivity to formation anisotropy. These advantages enable far more robust and accurate hypocenter inversion.

## ACKNOWLEDGMENTS

We are thankful to A. Malcolm, S. Chávez-Pérez, C. Oren, B. Witten, and three anonymous reviewers who dedicated their time and expertise to carefully evaluate our paper. We also want to thank Y. Zheng, R. Wang, and X. Chen for the insightful discussion on induced seismicity monitoring. We would like to express our gratitude to HighPeak Energy Inc., SM Energy, and Birch Resources for their great support in the field test and for providing the invaluable data used in this study.

## DATA AND MATERIALS AVAILABILITY

Data associated with this research are confidential and cannot be released.

## APPENDIX A

## IASP91 MODEL'S INVERSION QC RESULTS

Figures A-1–A-3, respectively, show events 1, 2, and 3 waveform alignment comparisons for the results inverted using the IASP91 model.

## APPENDIX B

## DB1D MODEL'S INVERSION QC RESULTS

Figures B-1–B-3, respectively, show events 1, 2, and 3 waveform alignment comparisons for the results inverted using the DB1D model.

**Table 4. Comparison of the local magnitudes (ML) reported by TexNet and recalculated based on our inverted event positions.**

| | Event 1 | Event 2 | Event 3 |
|---|---|---|---|
| Event ID | texnet2022qdqk | texnet2022qscz | texnet2022skdj |
| TexNet reported ML | 2.2 | 3.1 | 2.3 |
| Recalculated ML | 2.16 | 3.01 | 2.25 |
| ML change | −0.04 | −0.09 | −0.05 |

Note that the data of station 15 for event 2 and station 9 for event 3 are excluded in ML calculation due to poor data quality.

DOI:10.1190/geo2023-0238.1

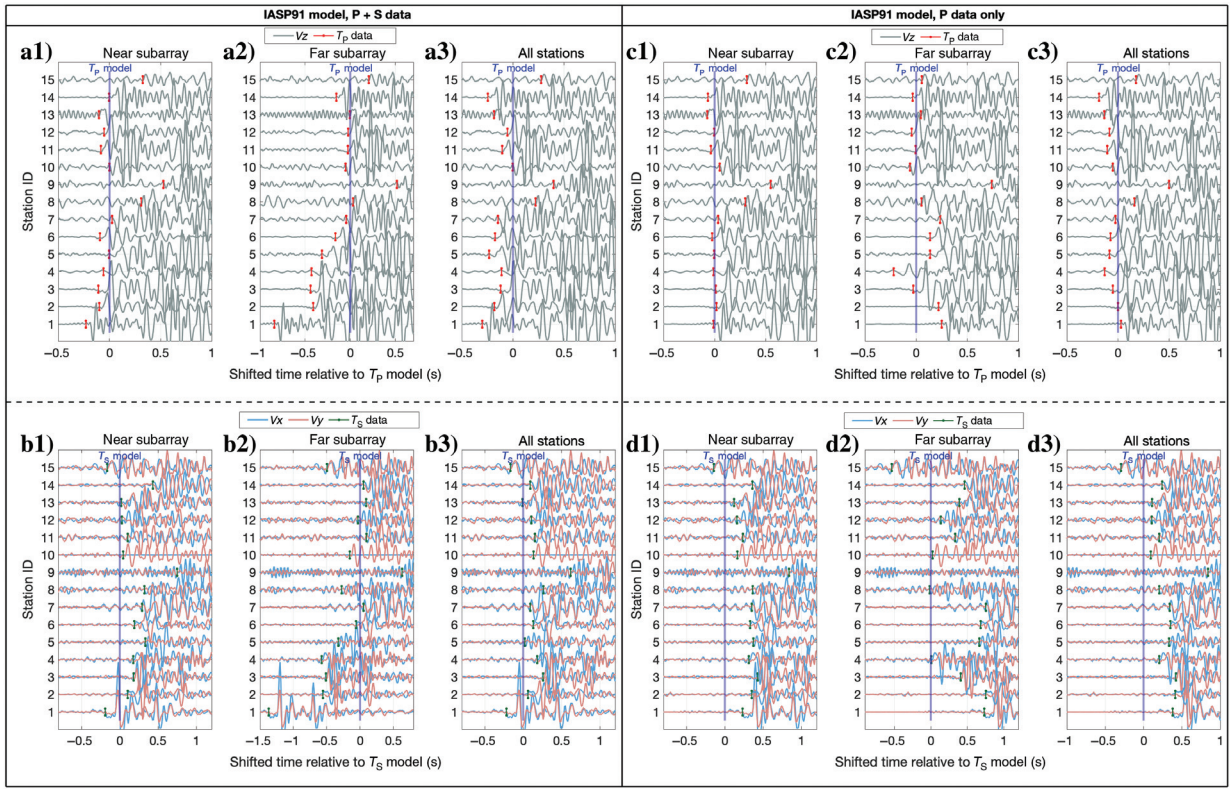


Figure A-1. (a1–a3 and b1–b3) and (c1–c3 and d1–d3) The results for event 1 inverted using P- and S-wave data and P-wave data only, respectively. In each panel, the first and second rows, respectively, show the vertical and horizontal components' waveforms with each trace's time zero shifted to the corresponding station's P-/S-wave modeled arrival times, which are calculated based on the hypocenters inverted from the data of near subarray, far subarray, and all stations using the IASP91 model. The vertical red and green bars, respectively, show the P- and S-wave first breaks picked from the data.

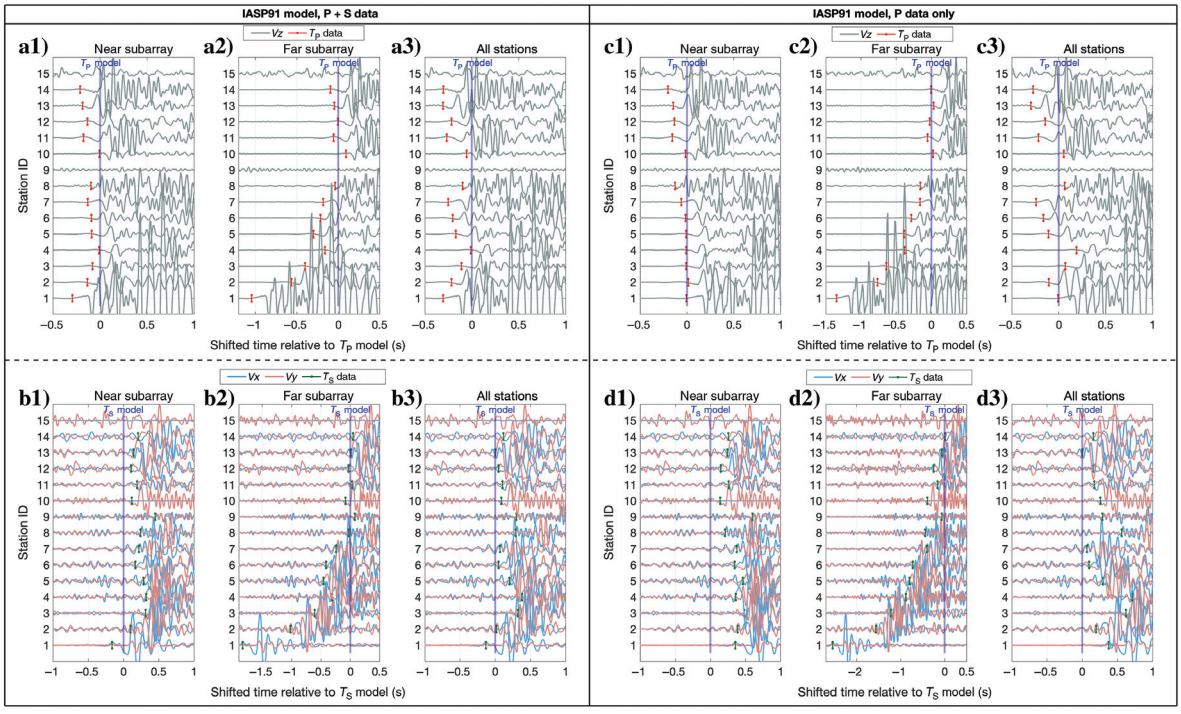


Figure A-2. Similar to Figure A-1, for comparisons of event 2 results inverted using the IASP91 model.

DOI:10.1190/geo2023-0238.1

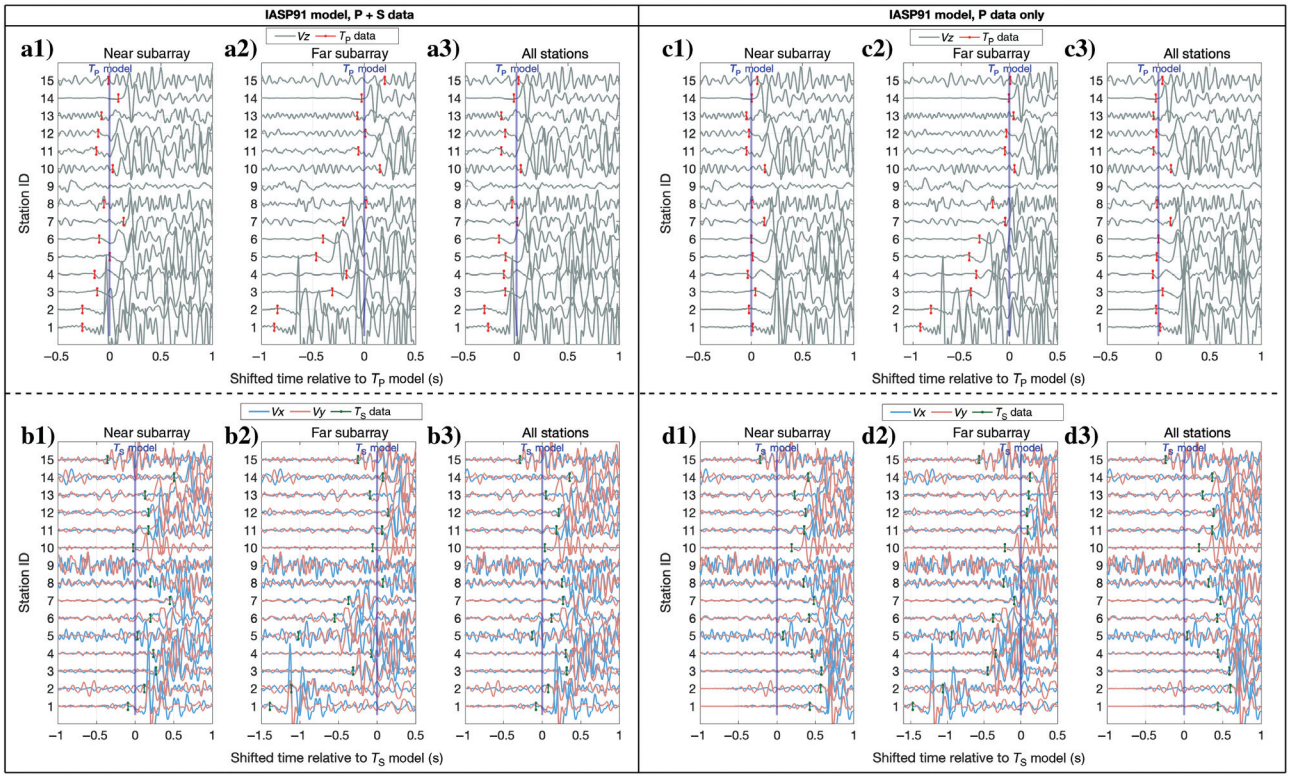


Figure A-3. Similar to Figure A-1, for comparisons of event 3 results inverted using the IASP91 model.

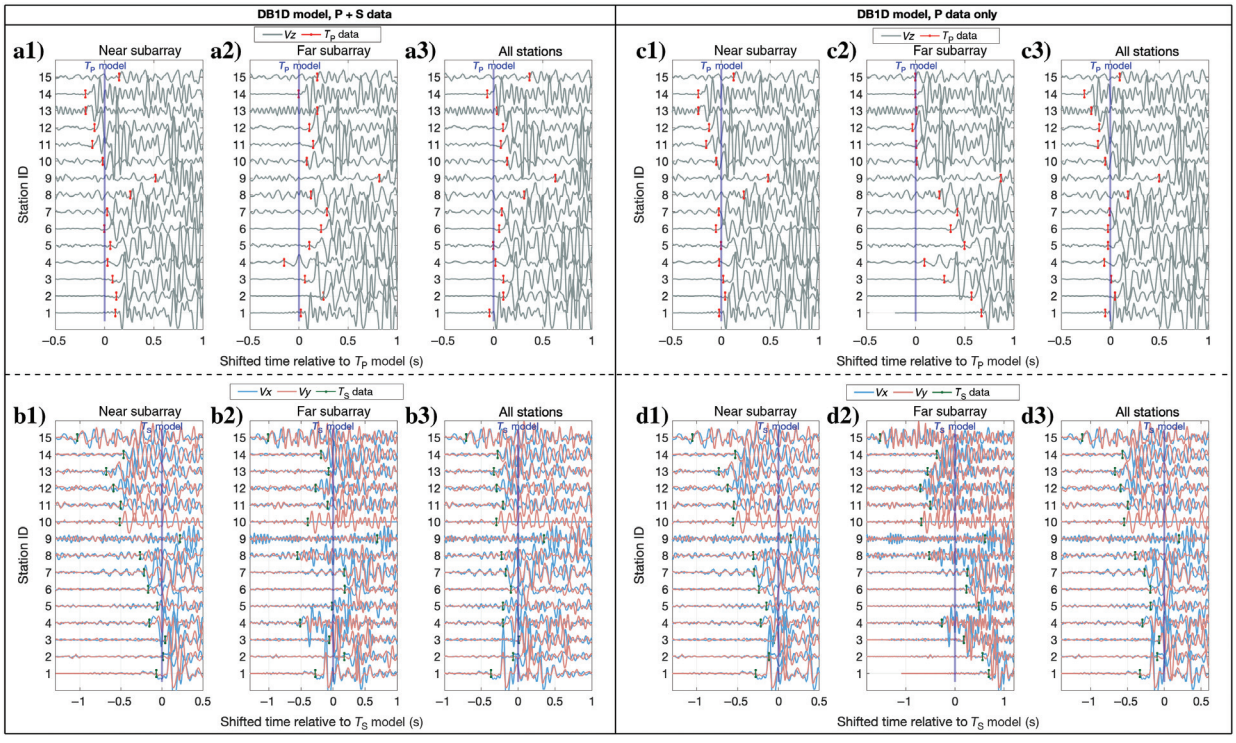


Figure B-1. (a1–a3 and b1–b3) and (c1–c3 and d1–d3) The results for event 1 inverted using P- and S-wave data and P-wave data only, respectively. In each panel, the first and second rows, respectively, show the vertical and horizontal components' waveforms with each trace's time zero shifted to the corresponding station's P-/S-wave modeled arrival times, which are calculated based on the hypocenters inverted from the data of the near subarray, far subarray, and all stations using the DB1D model. The vertical red and green bars, respectively, show the P- and S-wave first breaks picked from the data.

DOI:10.1190/geo2023-0238.1

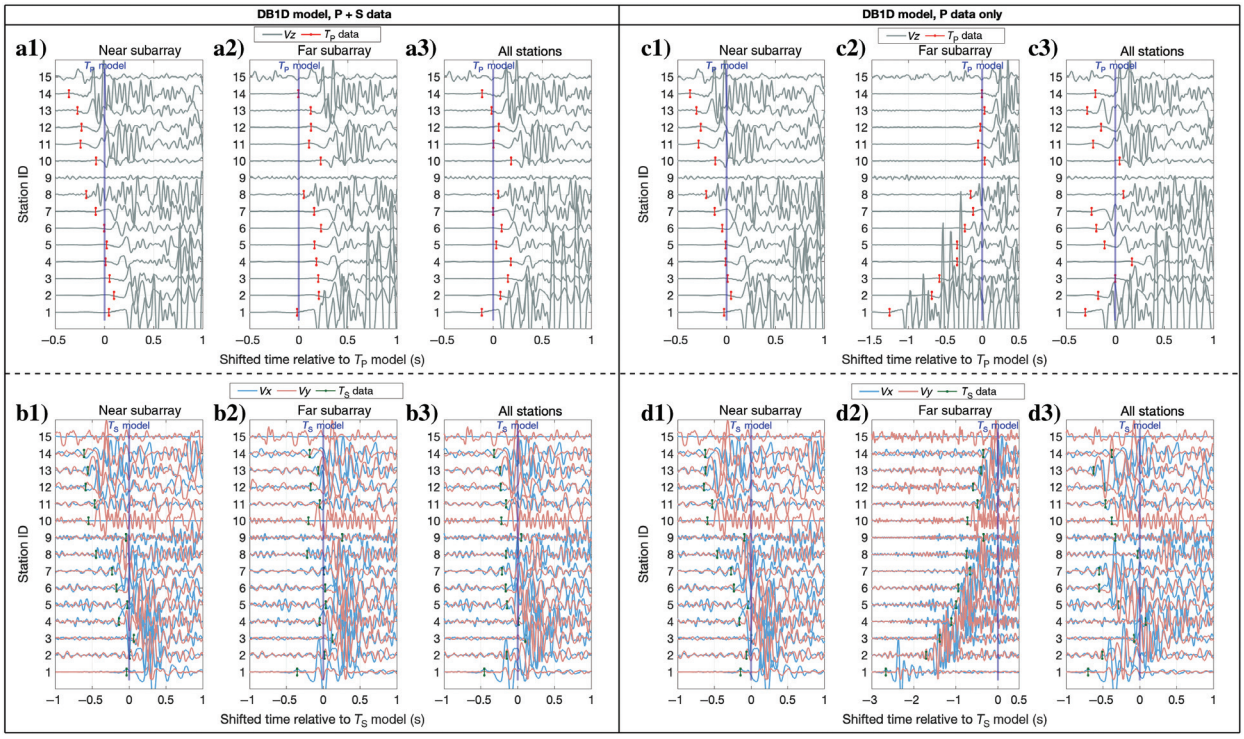


Figure B-2. Similar to Figure B-1, for comparisons of event 2 results inverted using the DB1D model.

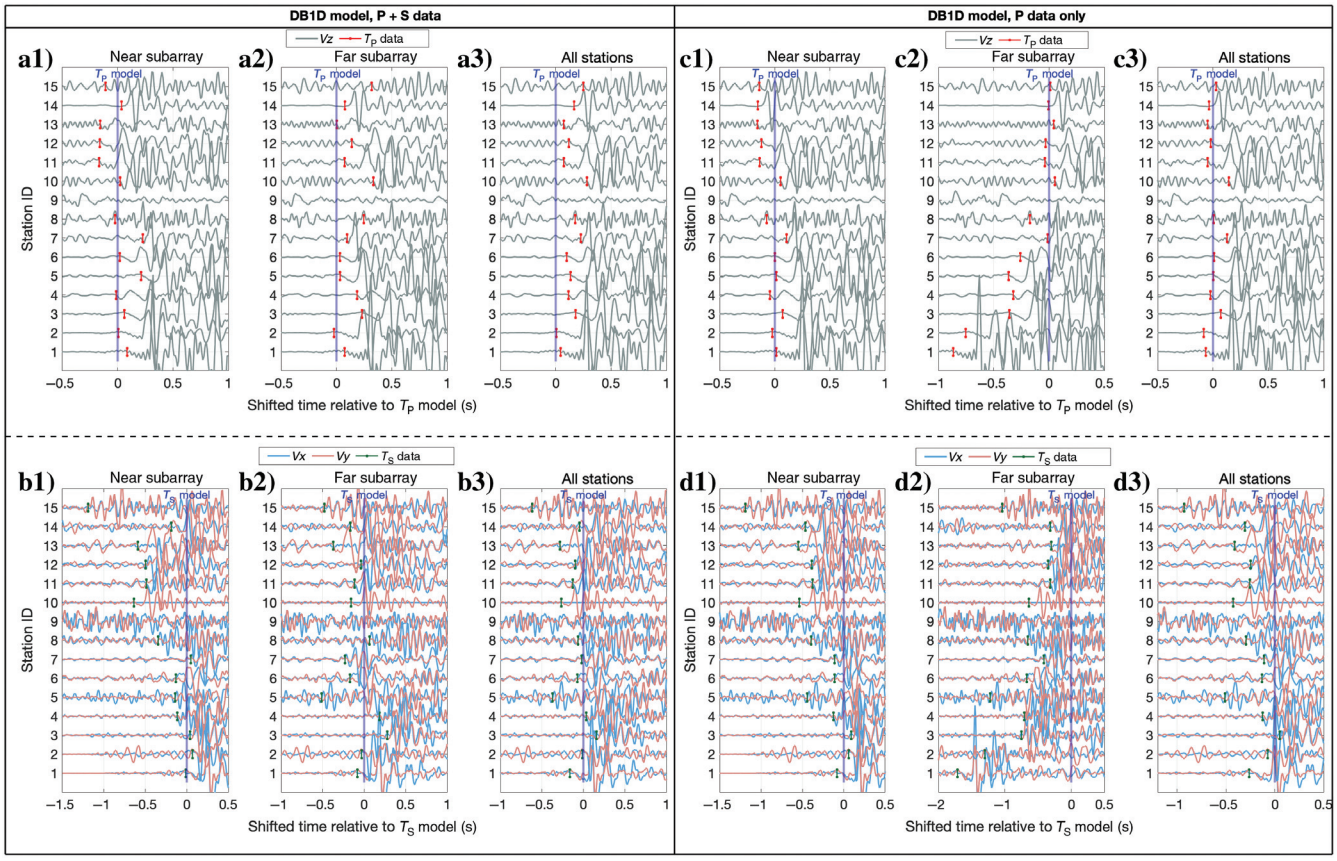


Figure B-3. Similar to Figure B-1, for comparisons of event 3 results inverted using the DB1D model.

DOI:10.1190/geo2023-0238.1

## REFERENCES


Aki, K., and P. G. Richards, 2002, Quantitative seismology, 2nd ed.: University Science Books.

Červený, V., L. Klimeš, and I. Pšenčík, 2007, Seismic ray method: Recent developments: Advances in Geophysics, **48**, 1–126, doi: 10.1016/S0065-2687(06)48001-8.

D'Alessandro, A., D. Luzio, G. D'Anna, and G. Mangano, 2011, Seismic network evaluation through simulation: An application to the Italian national seismic network: Bulletin of the Seismological Society of America, **101**, 1213–1232, doi: 10.1785/0120100066.

Deng, L., 1992, Seismic wave propagation in thinly layered media with steep reflectors: 62nd Annual International Meeting, SEG, Expanded Abstracts, 1260–1262, doi: 10.1190/1.1821966.

Duan, C., D. Lumley, and H. Zhu, 2022, Microearthquake location and uncertainty analysis using a Kirchhoff wavefront imaging method: A comparison with traveltime inversion and full wavefield imaging methods: Geophysics, **87**, no. 5, KS147–KS167, doi: 10.1190/geo2021-0699.1.

Fang, X., and X. Chen, 2019, A fast and robust two-point ray tracing method in layered media with constant or linearly varying layer velocity: Geophysical Prospecting, **67**, 1811–1824, doi: 10.1111/1365-2478.12799.

Frohlich, C., H. Deshon, B. Stump, C. Hayward, M. Hornbach, and J. I. Walter, 2016, A historical review of induced earthquakes in Texas: Seismological Research Letters, **87**, 1022–1038, doi: 10.1785/0220160016.

Hennings, P., N. Dvory, E. Horne, P. Li, A. Savvaidis, and M. Zoback, 2021, Stability of the fault systems that host-induced earthquakes in the Delaware Basin of West Texas and Southeast New Mexico: The Seismic Record, **1**, 96–106, doi: 10.1785/0320210020.

Kavoura, F., A. Savvaidis, and E. Rathje, 2020, Determination of local magnitude for earthquakes recorded from the Texas Seismological Network (TexNet): Seismological Research Letters, **91**, 3223–3235, doi: 10.1785/0220190366.

Kennett, B. L. N., and E. R. Engdahl, 1991, Travel times for global earthquake location and phase association: Geophysical Journal International, **105**, 429–465, doi: 10.1111/j.1365-246X.1991.tb06724.x.

Keranen, K. M., and M. Weingarten, 2018, Induced seismicity: Annual Review of Earth and Planetary Sciences, **46**, 149–174, doi: 10.1146/annurev-earth-082517-010054.

Li, L., J. Tan, B. Schwarz, F. Stanek, N. Poiata, P. Shi, L. Diekmann, L. Eisner, and D. Gajewski, 2020, Recent advances and challenges of waveform-based seismic location methods at multiple scales: Reviews of Geophysics, **58**, e2019RG000667, doi: 10.1029/2019RG000667.

Pepin, K. S., W. L. Ellsworth, Y. Sheng, and H. A. Zebker, 2022, Shallow aseismic slip in the Delaware basin determined by Sentinel-1 InSAR: Journal of Geophysical Research: Solid Earth, **127**, e2021JB023157, doi: 10.1029/2021JB023157.

Porritt, R. W., A. Savvaidis, B. Young, M. Shirley, and P. Li, 2020, Crustal structure in Southeastern Texas from joint inversion of ambient seismic noise and P to S receiver functions: Geochemistry, Geophysics, Geosystems, **21**, 1–13, doi: 10.1029/2019GC008866.

Savvaidis, A., B. Young, G. D. Huang, and A. Lomax, 2019, TexNet: A statewide seismological network in Texas: Seismological Research Letters, **90**, 1702–1715, doi: 10.1785/0220180350.

Schultz, R., R. J. Skoumal, M. R. Brudzinski, D. Eaton, B. Baptie, and W. Ellsworth, 2020, Hydraulic fracturing-induced seismicity: Review of Geophysics, **58**, e2019RG000695, doi: 10.1029/2019RG000695.

Schultz, R., R. Wang, Y. J. Gu, K. Huang, and G. Atkinson, 2017, A seismological overview of the induced earthquakes in the Duvernay play near Fox Creek, Alberta: Journal of Geophysical Research: Solid Earth, **122**, 492–505, doi: 10.1002/2016JB013570.

Schultz, R., J. Woo, K. Pepin, W. L. Ellsworth, H. Zebkar, P. Segall, Y. J. Gu, and S. Samsonov, 2023, Disposal from in situ bitumen recovery induced the ML 5.6 Peace River earthquake: Geophysical Research Letters, **50**, e2023GL102940, doi: 10.1029/2023GL102940.

Sheng, Y., K. S. Pepin, and W. L. Ellsworth, 2022, On the depth of earthquakes in the Delaware Basin: A case study along the Reeves-Pecos County line: The Seismic Record, **2**, 29–37, doi: 10.1785/0320210048.

Skoumal, R. J., A. J. Barbour, M. R. Brudzinski, T. Langenkamp, and J. O. Kaven, 2020, Induced seismicity in the Delaware Basin, Texas: Journal of Geophysical Research: Solid Earth, **125**, e2019JB018558, doi: 10.1029/2019JB018558.

Song, C., T. Alkhalifah, and Z. Wu, 2019, Microseismic event estimation and velocity analysis based on a source-focusing function: Geophysics, **84**, no. 3, KS85–KS94, doi: 10.1190/geo2018-0205.1.

Tang, L., and X. Fang, 2021, Generation of 6-C synthetic seismograms in stratified vertically transversely isotropic media using a generalized reflection and transmission coefficient method: Geophysical Journal International, **225**, 1554–1585, doi: 10.1093/gji/ggab044.

TexNet, 2023, TexNet earthquake catalog, https://www.beg.utexas.edu/texnet-cisr/texnet/earthquake-catalog, accessed 8 January 2023.

U.S. Geological Survey, 2023, United States geological survey earthquake catalog, https://earthquake.usgs.gov/earthquakes/search, accessed 8 January 2023.

Waldhauser, F., and W. L. Ellsworth, 2000, A double-difference earthquake location algorithm: Method and application to the northern Hayward fault, California: Bulletin of the Seismological Society of America, **90**, 1353–1368, doi: 10.1785/0120000006.

Zhai, G., M. Shirzaei, and M. Manga, 2021, Widespread deep seismicity in the Delaware Basin, Texas, is mainly driven by shallow wastewater injection: Proceedings of the National Academy of Sciences, **118**, 1–7, doi: 10.1073/pnas.2102338118.


Biographies and photographs of the authors are not available.